Field-aligned and ionospheric currents by AMPERE and SuperMAG during HSS/SIR-driven storms

M. N. Pedersen[1], H. Vanhamäki[1], A. T. Aikio[1], S. Käki[2,3], A. B. Workayehu[1], C. L. Waters[4], J. W. Gjerloev[5,6]

[1]Space physics and Astronomy Research Unit, University of Oulu, Oulu, Finland
[2]Finnish Meteorological Institute, Helsinki, Finland
[3]Division of Particle Physics and Astrophysics, University of Helsinki, Helsinki, Finland
[4]School of Mathematical and Physical Sciences, University of Newcastle, Callaghan, New South Wales, Australia
[5]The Johns Hopkins University Applied Physics Laboratory, Laurel, MD, USA
[6]Faculty for physics and technology, University of Bergen, Bergen, Norway

Key Points:

- Two peaks are observed in the auroral currents during HSS/SIR storms, first peak 40 min after storm onset and a second peak at $t_0 + 5.3$h.
- Both peaks are driven by SW-magnetosphere coupling as indicated by the ε parameter and the correlation coefficient between ε and FAC is 0.89.
- High p_{dyn} storms produce SSCs, larger SW coupling, the first peak in auroral currents, and a longer recovery phase than low p_{dyn} storms.

Corresponding author: Pedersen, M. N., marcus.pedersen@oulu.fi

Abstract

This study comprises 33 geomagnetic storms with Dst ≤ -50 nT driven by high-speed streams (HSSs) and associated stream interaction regions (SIRs) during 2010-2017. Their impact on ionospheric horizontal and field-aligned currents (FACs) have been investigated using superposed epoch analysis of SuperMAG and AMPERE data, respectively. The zero epoch (t_0) was set to the onset of the storm main phase. Storms begin in the SIR portion of the HSSs with enhanced solar wind density and compressed southward oriented magnetic field. The integrated FACs and horizontal currents have two peaks. The first and largest peak occurs at $t_0 + 40$ min and a second peak $t_0 + 5.3$ h, just before the Dst minimum. Both peaks are strongly driven by the solar wind, and the correlation between the Akasofu ε and integrated FAC is 0.89. The number of substorm onsets maximises near the storm onset. The storms were also separated into two groups based on the solar wind dynamic pressure p_{dyn} in the vicinity of the SIR. High p_{dyn} storms are driven by HSS/SIRs, where the solar wind velocity maximum is reached earlier and has shorter lead times to storm onset than low p_{dyn} events. The high p_{dyn} events also have sudden storm commencements, stronger solar wind driving and ionospheric response at t_0, and are primarily responsible for the first peak in the currents seen 40 min after t_0. After $t_0 + 2$ days, the number of substorm onsets becomes higher for low than high p_{dyn} events, which may be related to higher solar wind speed.

Plain Language Summary

Solar wind emanating from solar coronal holes tend to have faster velocity than the ambient solar wind and can together with southward oriented interplanetary magnetic field lead to geomagnetic storms in geospace. We have studied 33 geomagnetic storms of this kind and analysed the behaviour of the field-aligned currents and ionospheric horizontal currents in the high latitude auroral region with respect to the onset of the geomagnetic storms. We find that two peaks in the current systems occur during the storm main phase that are both strongly correlated and directly driven by the solar wind. We also split the storms into two groups based on the solar wind dynamic pressure at the onset of the storms. Several characteristic differences are found between the two groups, e.g. high pressure storms are largely responsible for the first peak in the currents and have shorter lead time between the coronal hole solar wind is detected by upstream satellites and the onset of the storm. These findings could help improve space weather predictions.

1 Introduction

Gonzalez et al. (1994) defined a geomagnetic storm as an interval of time when a sufficiently intense and long-lasting interplanetary convection electric field leads, through a substantial energization in the magnetosphere-ionosphere system, to an intensified ring current strong enough to exceed some key threshold of the quantifying storm time Dst index. The two processes responsible for causing the majority of storms are interplanetary coronal mass ejections (ICMEs) and high speed streams (HSSs) with their associated solar wind stream interaction regions (SIRs) (Kamide, Baumjohann, et al., 1998a,b).

HSS is solar wind emanating from coronal holes on the Sun with substantially higher velocity than the ambient solar wind (SW) (Krieger et al., 1973; Neupert & Pizzo, 1974). At the interface between the slow and fast SW, a region of compressed density and interplanetary magnetic field (IMF) develops that is often accompanied by a change in direction of the SW flow velocity (Gosling et al., 1978). These regions are known as SIRs, or co-rotating interaction regions (CIRs) if the coronal hole persists for more than one solar rotation (Balogh et al., 1999; Jian et al., 2006). Some papers (e.g. Jian et al., 2006) use the term SIR for interaction regions that are only seen during one solar rotation, as opposed to the longer lasting CIR, but in this article we use the term SIR for any stream interaction region, re-

gardless of the duration. HSS/SIRs occur most frequently during the declining phases of solar cycles (Gonzalez et al., 1999; Tsurutani et al., 2006; Grandin et al., 2019) and are the most frequent sources of weak-to-moderate (Dst>-100 nT) storms (Zhang et al., 2008; Richardson & Cane, 2012). In contrasts, ICMEs are the most common source of large and major (Dst<-100 nT) storms and are most frequently observed during solar cycle maxima (Webb & Howard, 1994; Borovsky & Denton, 2006).

Although ICMEs give rise to the strongest storms, HSS/SIRs typically are of longer duration and have longer lasting impact on the Earth's magnetosphere-ionosphere-thermosphere (MIT) system (Turner et al., 2009; Burns et al., 2012). The presence of Alfvénic fluctuations have been observed in the SW of HSS/SIRs. This Alfvénic activity consists of large-amplitude quasi-periodic fluctuations in the orientation of the IMF with periods ranging from tens of minutes to a few hours (Belcher & Davis Jr, 1971; Kamide, Baumjohann, et al., 1998b; Tanskanen et al., 2017). Alfvénic activity in HSS/SIR storms can prolong the storm recovery phase by allowing for frequent and recurring reconnection between the SW and magnetosphere that in turn drives substorms. This type of substorms and ionospheric current activity is known as high intensity, long duration continuous auroral activity (HILDCAA) events (Tsurutani & Gonzalez, 1987).

A magnetic storm usually contains many individual magnetospheric substorms. During substorms, both horizontal currents and Birkeland currents, also known as field-aligned currents or FACs, intensify. Several studies have focused on the connection between substorms and the ionospheric currents (e.g. Coxon et al., 2014a; McPherron et al., 2018). Coxon et al. (2014b) reported results from a superposed epoch analysis (SEA) study of substorms, where they analysed the magnitude and spatial evolution of the Region 1 (R1) and Region 2 (R2) FACs and found that each current system increased in magnitude by up to 1.25 MA over the course of a substorm cycle.

The statistical patterns of Birkeland currents have been studied in several papers, and they are typically presented as a function of the IMF direction and magnitude, although other parameters may be used (Iijima & Potemra, 1978; Weimer, 2001; Anderson et al., 2008; Juusola et al., 2009; Laundal et al., 2018; Workayehu et al., 2020). Anderson et al. (2005) stated that "While statistical patterns of Birkeland currents are well known, we know little about their storm-time characteristics, in part because storm-time current systems do not repeat in the same sequence from storm to storm". The main aim of our study is to address this question for HSS/SIR-driven storms. In addition, we also study the evolution of horizontal equivalent currents in the ionosphere.

Numerous studies have considered the impact of IMF, the solar wind electric field E_Y or some other coupling function depending on IMF direction, magnitude and solar wind velocity on the magnetosphere and ionosphere, as these are the main parameters governing solar wind-magnetospheric coupling (see e.g Dungey, 1961; Rostoker & Fälthammar, 1967; Akasofu, 1981, and references therein). Korth et al. (2010) studied the effect that different SW and IMF parameters have on the intensity of the FACs and found that the impact of SW dynamic pressure was modest compared to E_Y. It has been found that the dynamic pressure has the most prominent impact on the magnetosphere-ionosphere-thermosphere system under steady B_Z negative orientation (e.g. Boudouridis et al., 2003, 2004, 2005). Solar wind dynamic pressure has been omitted in many solar wind-magnetosphere energy coupling functions, as it had long been thought to not play a major role in the energy transfer (Akasofu, 1981), but later studies (e.g. Newell et al., 2008) have shown that including the dynamic pressure can make significant improvements in the predictions.

In this study, we examine the effect HSS/SIR driven storms have on the temporal and spatial evolution of FACs and ionospheric currents on time scale of storms ($\sim$ days) using the global FAC and ionospheric equivalent current provided by the Active Magnetosphere and Planetary Electrodynamics Response Experiment (AMPERE) (Anderson et al., 2000, 2002; Waters et al., 2001, 2020) and SuperMAG (Gjerloev, 2009, 2012), respectively. We use

data from 33 HSS/SIR storms with Dst ≤ -50 nT that occurred during 2010-2017 and use a superposed epoch analysis to study the auroral current systems in the northern hemisphere. We also study the effect of solar wind dynamic pressure on the auroral current systems in the vicinity of the SIR.

The structure of the paper is as follows: section 2 describes the event selection process and the data analysis methods. Section 3 shows the results in three parts: in 3.1 we analyse all the events and report their spatial and temporal evolution during the HSS/SIR driven storms, in 3.2, we separate the storms into low and high SW dynamic pressure events and study its impact on the currents, and in 3.3 describe the correlation between the FACs, AE and Akasofu ε. Section 4 is a discussion of the results and section 5 gives a summary and conclusion of our findings.

2 Data, event selection and analysis method

2.1 Data

Data from AMPERE, SuperMAG and the OMNIWeb have been used. The AMPERE project provides fitted FAC densities in the high latitude region derived from magnetic field perturbations measured onboard the Iridium Communication satellite constellation of more than 70 satellites in near-polar orbit (Anderson et al., 2000, 2002; Waters et al., 2001, 2020). SuperMAG provides gridded ground magnetic field perturbation vectors from magnetometer measurements around the globe (Gjerloev, 2009, 2012; Waters et al., 2015). SuperMAG also provides a list of substorm onsets derived from an automated algorithm using the SML index; the SuperMAG equivalent of the AL index (Newell & Gjerloev, 2011b,a). The OMNIWeb service provides data of the solar wind and geomagnetic indices (King & Papitashvili, 2005). The Dst index is also taken from the OMNIWeb service. Since Dst is a 1 h index, all the analysis and plots use the center of the 1 h window as a time tag.

Only data from the northern hemisphere is used. This is because there are less ground magnetometer stations located in the southern hemisphere and the AMPERE FAC densities may be less reliable due to the larger offset between the Earth's geomagnetic and geographic south pole (e.g Anderson et al., 2002), making the intersection point of Iridium satellite orbits to often be in the southern auroral oval.

2.2 Selecting HSS/SIR-driven geomagnetic storms

The search for HSS/SIR-driven storms were limited to $2010 - 2017$, as that is the period when both AMPERE and SuperMAG was operational. Events were selected based on the geomagnetic storm criteria by Partamies et al. (2013) as described below. Storms are typically categories as weak (-50 nT $<$ Dst <-30 nT), moderate (-100 nT $<$ Dst<-50 nT) and strong (Dst < -100 nT) (Gonzalez et al., 1994; Loewe & Prölss, 1997, e.g.). We only include storms that are moderate or strong, therefore we use the additional condition that the Dst index must reach at least -50 nT. The storm main phase onset time was set to the time when the Dst index decreased below -15 nT. The main phase ended when the Dst index reached minimum, which must be ≤ -50 nT. The recovery phase lasted from the Dst minimum until the Dst index had reached -15 nT. All the storms found using the above algorithm were compared with the HSS/SIR list by Grandin et al. (2019), and only storms that had a main phase onset during the time of a HSS/SIR event were selected. Grandin et al. (2019) in their HSS/SIR list removed any candidates, which were likely affected by an ICME event by comparing the arrival time of the HSS to ICME events from Richardson & Cane (2010) (http://www.srl.caltech.edu/ACE/ASC/DATA/level3/icmetable2.htm - link to more frequently updated Richardson's and Cane's ICME list). In total 140 storms with Dst ≤ -50 nT between 2010 and 2017 were detected, of which 51 were HSS/SIR-related. Of these 51 storms there is full AMPERE data coverage for 33 storms, which form the dataset for our study. Table 1 lists the main characteristics of the selected storms.

Figure 1 shows the yearly distribution of the storms and the durations of the main and recovery phases. The majority of the storms took place after 2015, during the declining phase of solar cycle 24. The monthly distribution of the storms (not shown here) peaked with seven storms in March followed by four in April and the remaining of the months all had between one and three storms. Strong storms are more likely to occur close to the equinoxes, which can be explained by the dipole axial tilt, the Russel-McPherron effect (Russell & McPherron, 1973) and equinoctial effect (Cliver et al., 2000).

Twenty-six of the 33 storms had a main phase duration of less than 10 h and the median duration was 6 h, with interpolated lower and upper quartiles of 4.75 h and 9.25 h, respectively. The two longest events (#6 and #30) were compound events that involved a local Dst minimum ≤ -50 nT before reaching a second deeper Dst minimum resulting in the long main phase durations (81 h and 123 h, respectively). These events still fit nicely into our study as the first Dst minimum is ≤ -50 nT (-64 nT at 5 h and -59 nT at 40 h after main phase onset for storms 6 and 30, respectively) and we limit the superposed epoch analysis to the first 60 hours after zero epoch. In individual storms, the median recovery phase duration was 60 h and the interpolated lower and upper quartiles were 35.75 h and 94.0 h, respectively.

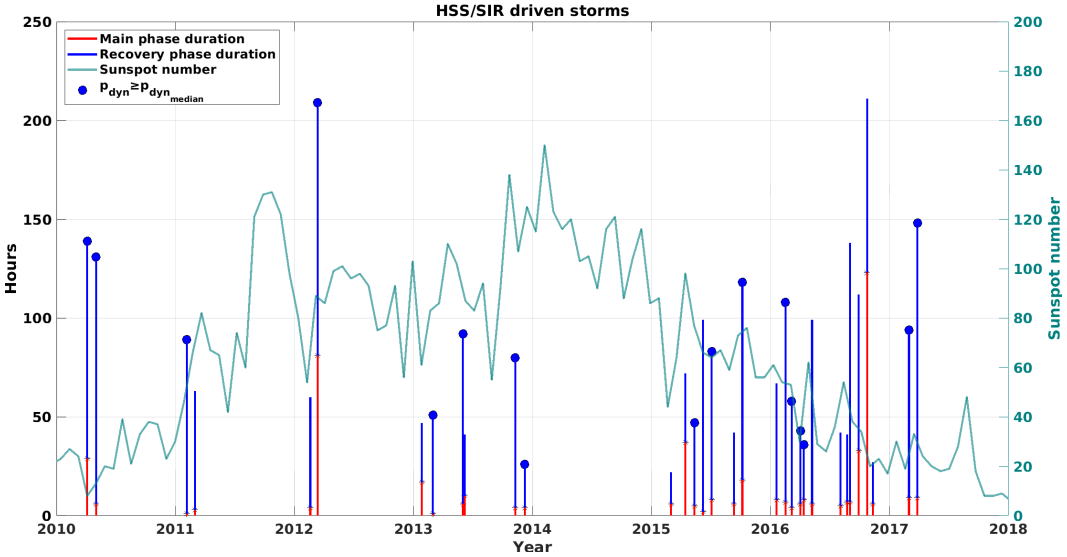

Figure 1: Distribution of the 33 HSS/SIR related storms. Red line shows the main phase duration of the storm and blue line the recovery phase duration (left axis). Storms with circles at the top of the lines are high dynamic pressure events (see section 3.2). The 27-day average sunspot number is also shown (right axis).

2.3 Data analysis methods

The fitted AMPERE data product is provided at 2 minute cadence over a 10 min window. We used the data at 10 minute temporal resolution, meaning all measurements are independent. The spatial resolution is 1 h magnetic local time (MLT) and 1° magnetic latitude (MLAT) in altitude adjusted corrected geomagnetic (AACGM) coordinates (Baker & Wing, 1989). The gridded SuperMAG magnetic field perturbation vectors have 1 min time resolution and spatial resolution is 1 MLT hour and 2° MLAT (Waters et al., 2015).

Table 1: List of the 33 HSS/SIR storms in our study. Onset times given in UT.

Storm number	Low/High p_{dyn}	Main phase onset (zero epoch)	Main phase duration (h)	Recovery phase duration (h)	Dst minimum (nT)
1	High	05-Apr-2010 09:30	29	110	-81
2	High	02-May-2010 12:30	6	125	-71
3	High	04-Feb-2011 20:30	1	88	-63
4	Low	01-Mar-2011 11:30	3	60	-88
5	Low	19-Feb-2012 00:30	4	56	-63
6	High	12-Mar-2012 11:30	81	128	-88
7	Low	26-Jan-2013 05:30	17	30	-51
8	High	01-Mar-2013 09:30	1	50	-55
9	High	01-Jun-2013 02:30	6	86	-124
10	Low	06-Jun-2013 16:30	10	31	-78
11	High	09-Nov-2013 04:30	4	76	-80
12	High	08-Dec-2013 04:30	4	22	-66
13	Low	02-Mar-2015 02:30	6	16	-54
14	Low	15-Apr-2015 10:30	37	35	-79
15	High	13-May-2015 01:30	5	42	-76
16	Low	08-Jun-2015 06:30	2	97	-73
17	High	04-Jul-2015 21:30	8	75	-67
18	Low	11-Sep-2015 08:30	6	36	-81
19	High	07-Oct-2015 04:30	18	100	-124
20	Low	20-Jan-2016 08:30	8	59	-93
21	High	16-Feb-2016 12:30	7	101	-57
22	High	06-Mar-2016 17:30	4	54	-98
23	High	02-Apr-2016 17:30	6	37	-56
24	High	12-Apr-2016 21:30	8	28	-55
25	Low	08-May-2016 02:30	6	93	-88
26	Low	03-Aug-2016 05:30	5	37	-52
27	Low	23-Aug-2016 14:30	7	34	-74
28	Low	01-Sep-2016 02:30	7	131	-59
29	Low	28-Sep-2016 00:30	33	79	-66
30	Low	24-Oct-2016 00:30	123	88	-64
31	Low	10-Nov-2016 11:30	6	21	-59
32	High	01-Mar-2017 12:30	9	85	-61
33	High	27-Mar-2017 05:30	9	139	-74

The OMNI SW and IMF data, mapped to the bowshock, have a time resolution of 1 h. The data processing is described in the following subsections.

2.3.1 Superposed epoch analysis

The storm properties and auroral currents were studied using a superposed epoch analysis (SEA) approach. In SEA, the time series of a given parameter were overlapped using the same zero epoch time and then the median and quartiles were extracted. We used the median and quartiles instead of mean and standard deviation as they are less affected by outliers. The zero epoch (t_0) was set to the onset of the storm's main phase, defined as the time when the Dst index first decreased to below -15 nT (Partamies et al., 2013). The choice of t_0 can have implications on the characteristic behavior of the parameters being studied (Ilie et al., 2008), and therefore it is important to choose an appropriate t_0 for the phenomena of interest. This study focuses on exploring both the temporal and spatial variability of the ionospheric currents during the most active periods of the HSS/SIR storms, and therefore choosing the storm main phase would allow us to see the general evolution as the storm develops. In the SEA, the time window chosen was from 12 h before t_0 until 60 h (2.5 days) afterwards. This time window includes information on the pre-storm condition of the current systems and in the majority of the storms the activity level had relaxed close to the normal time conditions within 2.5 days.

2.3.2 FACs from AMPERE

In order to reveal the spatial variation, hemispheric maps were constructed by superposing the currents at each MLAT/MLT grid cell, i.e. at each timestep the median value of the 33 storms in each grid cell is shown:

$$J_{ij}(t) = \text{median}\left(J_{Nij}(t)\right), \qquad \text{for } N = 1, 2, ..., 33 \tag{1}$$

where t is the time from zero epoch, N is the storm number and i and j are the MLAT and MLT coordinates, respectively.

In addition to the superposed maps, time series of the integrated FACs in each storm and their superposition were also investigated. To maintain information about the upper and lower quartiles of the integrated FAC, the upward and downward FAC densities were processed separately for each storm:

$$J^{+}_{Nij}(t) = \begin{cases} J_{Nij}(t) & \text{if } J_{Nij}(t) > 0 \\ 0 & \text{else} \end{cases} \tag{2}$$

$$J^{-}_{Nij}(t) = \begin{cases} J_{Nij}(t) & \text{if } J_{Nij}(t) < 0 \\ 0 & \text{else} \end{cases} \tag{3}$$

where positive values represent the upward currents and negative values the downward currents. When integrating the FACs, any current J with an absolute magnitude less than 0.16 μA/m^2 was set to zero. Anderson et al. (2014) found 0.16 μA/m^2 to be three times the standard deviation of the quiet time current density. Therefore, by removing these small currents, the integration was restricted to only include statistically significant FACs. Then, the total upward or downward integrated FAC for a given storm became:

$$I_N^{\pm}(t) = \sum_{\text{i=MLAT}} \sum_{\text{j=MLT}} A_{ij} J_{N_{ij}}^{\pm}(t). \tag{4}$$

Here the FAC density was multiplied with the area of each grid cell, A_{ij}. The summation was carried out from 40° to 90° MLAT and all MLTs. The grid sizes are 1° MLAT and 1 h MLT. The timestep is 10 min and calculation was carried out between $t_0-0.5$ d and $t_0+2.5$ d. After the integrated FACs had been calculated for each event, they were added to SEA to yield the total FAC versus SEA time.

Later, the total integrated currents were separated into four different MLT sectors, noon (09-15 MLT), dusk (15-21 MLT), midnight (21-03 MLT) and dawn (03-09 MLT), to allow for study of the behaviour in the different regions.

2.3.3 Equivalent currents from SuperMAG

The magnetic field vectors from SuperMAG were rotated clockwise by 90° to represent the horizontal equivalent currents. The units have not been converted from nT to A to emphasis that we use the ground-magnetic perturbations. Gjerloev & Hoffman (2014) did an analysis of the SuperMAG data in a similar fashion, and pointed out a simple relation between ground measured magnetic perturbation and current: 1 nTkm roughly corresponding to 2 A equivalent current (Kamide et al., 1982). Equivalent currents represent the divergence-free part of the height-integrated current, which can often be approximated as the Hall current. In the analysis of the electrojet currents, we separated the vectors into southward and northward magnetic field perturbations, to represent the westward and eastward horizontal currents, respectively. The integration was carried out from $54-76°$ MLAT across all included MLTs, then divided by the number of MLTs to show the average eastward electrojet (EEJ) and westward electrojet (WEJ) current. In order to maintain information about the upper and lower quartiles in the EEJ and WEJ currents, the integration and superposed epoch analysis was calculated separately for the different current directions, similar to the upward and downward FACs discussed in Section 2.3.2.

2.3.4 Solar wind parameters

The SW and IMF parameters are delayed to the magnetospheric bowshock with 1 h time resolution in the OMNI data base. Two additional quantities were derived using the OMNI data, the solar wind dynamic pressure $\mathrm{p_{dyn}}$ and Akasofu ε parameter (Akasofu, 1981). The solar wind dynamic pressure is:

$$\mathrm{p_{dyn}} = m_p \rho_{SW} V_{SW}^2 \tag{5}$$

where m_p is the proton mass, ρ_{SW} is the upstream SW density and V_{SW} is the SW speed. Akasofu ε is one of the most widely used coupling functions, describing energy coupling between the solar wind and the magnetosphere. Akasofu ε is defined as:

$$\varepsilon(\mathrm{W}) = \frac{4\pi}{\mu_0} V_{SW} B^2 \sin^4\left(\frac{\theta}{2}\right) l_0 \tag{6}$$

where B is the IMF magnitude, θ the IMF clock-angle and l_0 the reconnection line at the dayside magnetopause taken with the empirical value of 7 R_E from Akasofu (1981).

3 Results

In this section, all the 33 storms are first studied together to see what kind of SW conditions and currents can be expected from a typical HSS/SIR driven storms. Then the storms are split into two groups based on the SW dynamic pressure and the differences in the SW driving, FACs and ionospheric currents are investigated. The last part of this section focuses on the correlation between the FACs, AE index and solar wind coupling for all the storms and the different dynamic pressure groups.

3.1 Superposed epoch analysis of all HSS/SIR storms

Figure 2 shows the superposed SW OMNI data for all of the storms. The first three panels are the SW dynamic pressure, velocity and density. These panels show that the majority of the storms begin before the velocity reaches 500 km/s, during the time of large plasma compression in the SIR. The following three panels show SW proton density, IMF B_Z component, IMF scalar value and Akasofu ε coupling function. Zero epoch (the time when the Dst index decreases below -15 nT) coincides with the minimum B_Z and maximum IMF B magnitude. The negative B_Z is one of the important driving parameters allowing for solar wind-magnetosphere coupling and increased B magnitude can be associated with enhanced plasma density in the SIR portion of the HSS. Last panel shows that the coupling between the solar wind and magnetosphere starts to increase rapidly two hours prior to t_0 and reaches maximum at t_0, followed by a period of steady elevated coupling and a second smaller peak 5 h after t_0 (mainly visible in the upper quartile).

A polar MLT/MLAT overview of the superposed AMPERE FACs and SuperMAG equivalent currents in the northern hemisphere at six different times are shown in Figure 3. The color shading shows the field-aligned upward (positive) and downward (negative) current density, and the arrows show 90° rotated magnetic field perturbation vectors - red arrows are eastward currents and blue arrows are westward currents. Panel a) is 12 h before t_0 and shows the pre-storm condition of the FAC and electojet currents, with very small values. Panel b) is taken 2 h before t_0, and some enhancement can already be observed in both the FACs and electrojets. The FAC enhancement is observed in all MLT sectors, while all the equivalent currents above 60° MLAT are increased with the largest values in the morning and midnight sectors where the WEJ flows. The magnetic Harang discontinuity can be identified to be located at 22 MLT below 68° MLAT, shifting westward by one MLT hour per 2° MLAT up to 74°.

Panel c) shows that at t_0, major enhancements are observed in both the FAC and electrojet currents, and the Harang discontinuity has moved to 21 MLT below 68° MLAT. The spatial distribution of the FAC system displays the well known R1/R2 currents (Iijima & Potemra, 1978), with the polarward R1 oriented upward (downward) in dusk (dawn) and the equatorward R2 currents having opposite directions than R1 in the same MLT sectors. The maximum R1 current densities are observed at 17-18 MLT and at 68° MLAT (upward) and at 07-08 MLT and 72° MLAT (downward). The WEJ has intensified and extended to become dominant in the midnight sector.

Panel d) at t_0 + 40 min shows the auroral currents at the time of maximum superposed integrated FAC (determined from Figure 4 discussed below), and is 18 minutes earlier than maximum superposed integrated horizonal equivalent currents that peak at t_0+58 min. The WEJ in the dawn and midnight sectors and the EEJ in the dusk sector are larger than at t_0 and have expanded $\sim 2°$ further equatorwards. In the dusk sector enhancement in the westward equivalent current is seen at mid-latitudes between $40-52°$ MLAT. These are likely not real ionospheric currents, but disturbances from the asymmetric ring current and/or magnetopause current that also increases during times of geomagnetic activity (Newell & Gjerloev, 2012; Haaland & Gjerloev, 2013).

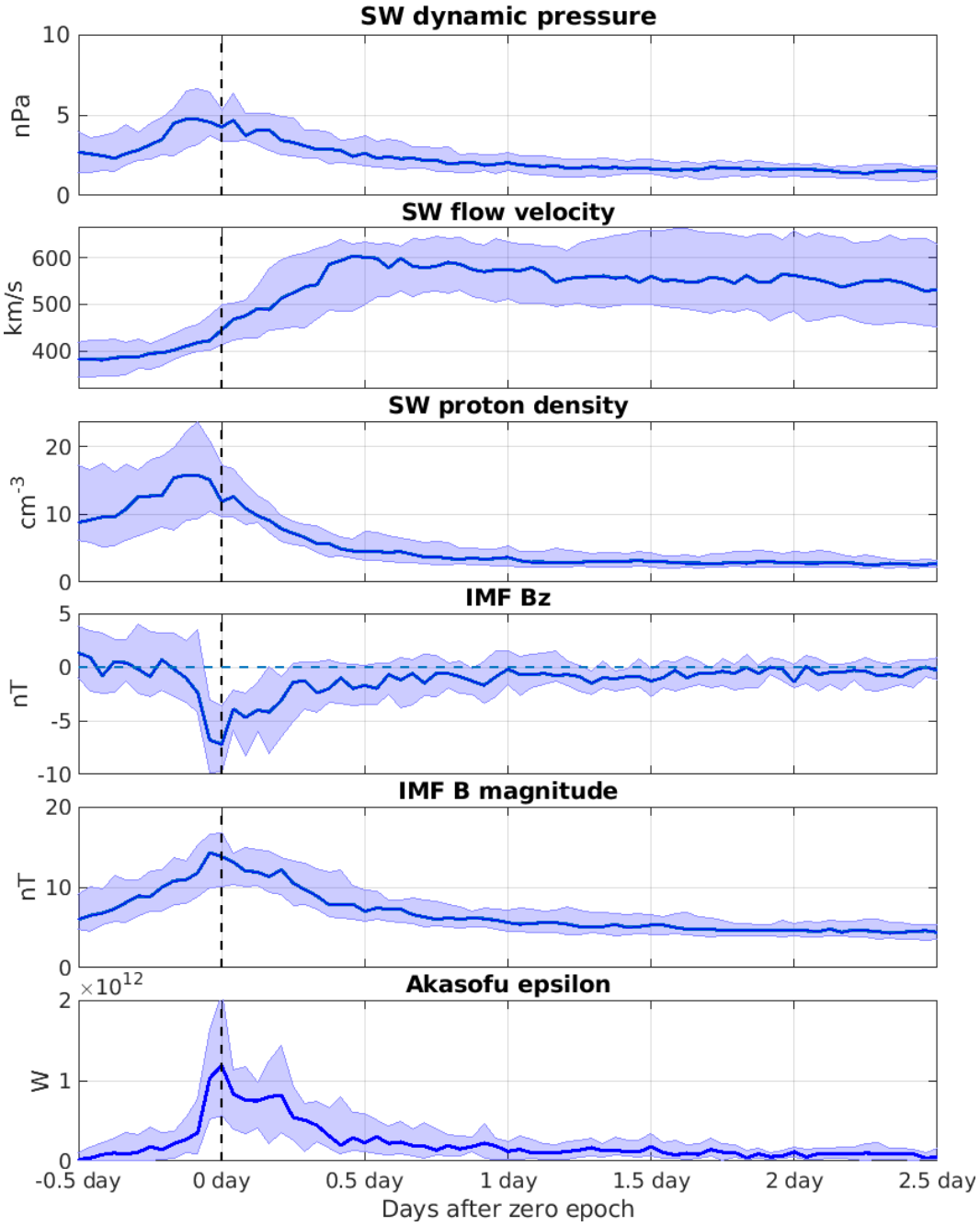

Figure 2: From top to bottom panel are the superposed solar wind dynamic pressure, flow velocity, density, northward IMF B_Z-component, IMF B magnitude and Akasofu ε for all the 33 storms in our study. The solid line shows the median superposed value and the shaded area indicates the upper and lower quartiles. The dashed vertical line shows the time of zero epoch.

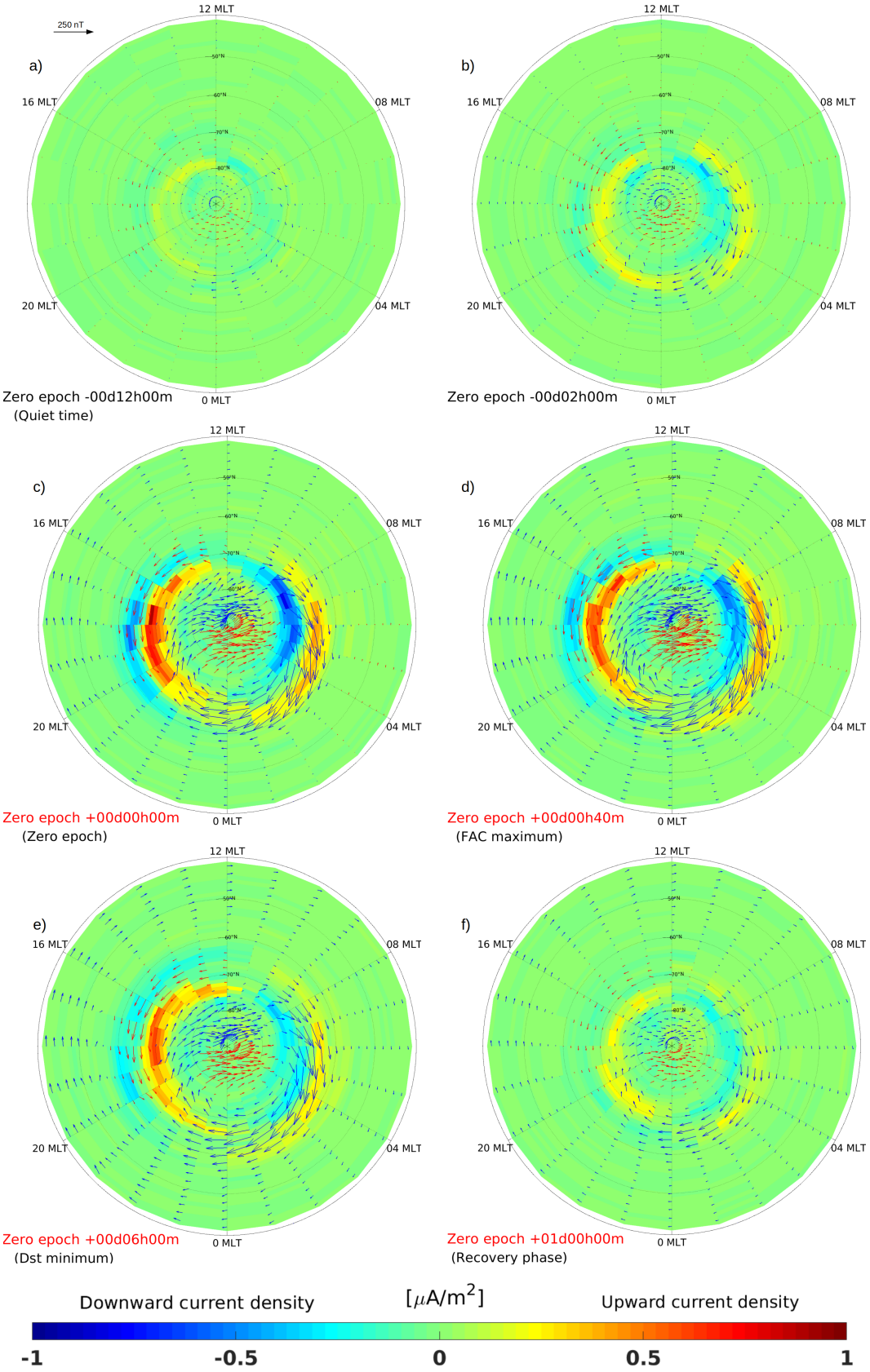

Figure 3: Superposed AMPERE FAC density and rotated SuperMAG magnetic field perturbation vectors for all the geomagnetic storms at six different times with respect to zero epoch plotted in AACGM coordinates.

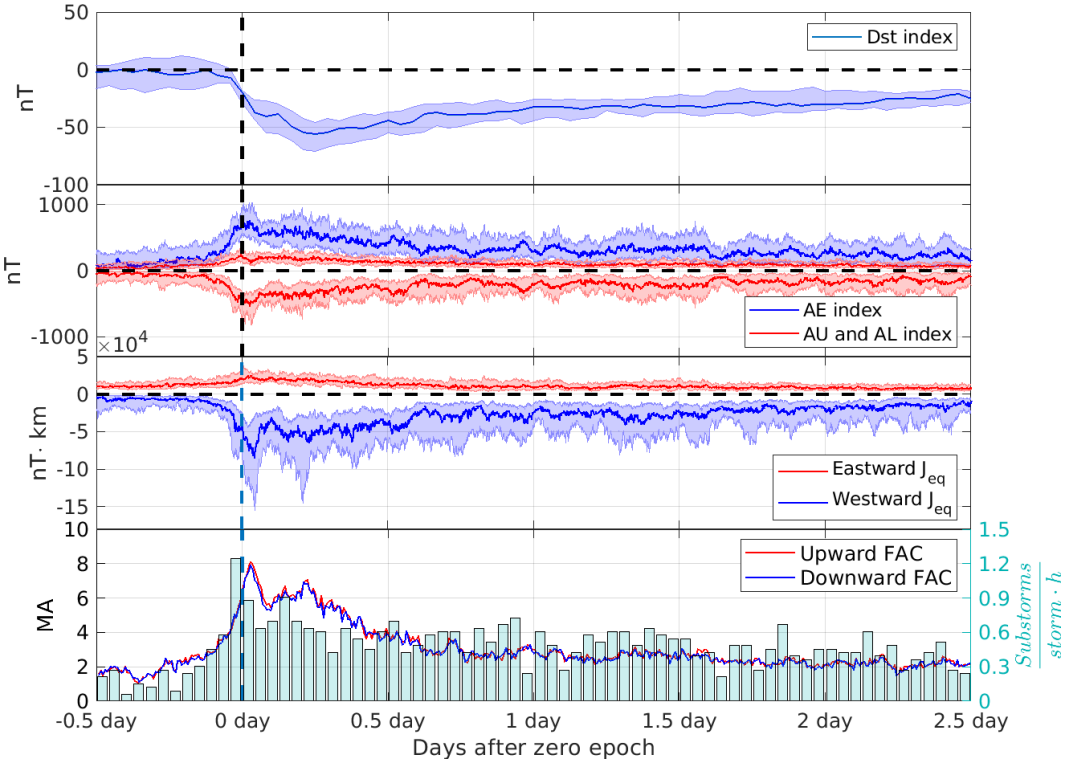

Figure 4: Top panel show the superposed Dst index. The second panel is the superposed AE, AU and AL index. The third panel shows the superposed integrated SuperMAG J_{eq}. In the bottom panel is the total integrated FAC with bars showing the number of average substorm onsets pr storm occurring in 1-hour bins. The shaded areas shows the upper and lower quartiles of the superposed values.

Panel e) shows the time of superposed Dst minimum and is the time the mid-latitude disturbance maximizes. At this time the magnitudes of the FAC and equivalent currents have reduced compared to panel d), but the extent of the WEJ in the midnight sector has moved equatorward by $\sim 4°$ compared to t_0.

Panel f) is 24 h after t_0, in the middle of the recovery phase. The FAC and WEJ, but not the EEJ, are still larger than at t_0 - 2 h shown in panel b), with the Harang discontinuity still at 21 MLT below 68° MLAT. The mid-latitude equivalent currents remain more prominent 24 h after t_0 than what was seen in b) 2 h before t_0, and could therefore account for a reduction in dusk side EEJ currents and slightly skew the Harang discontinuity westward at the lower boundary of the auroral oval.

Figure 4 shows the superposed Dst index, the superposed AE, AU and AL indices, the superposed integrated J_{eq} and the superposed total integrated FAC, separately for upward and downward currents, with the number of substorm onsets from the SuperMAG onset list (Newell & Gjerloev, 2011a). The superposed Dst index decreases in two steep slopes, with the first spanning from t_0 - 1 h until t_0 + 1 h and the second from t_0 + 3 h until the Dst minimum at t_0 + 6 h. The AE indices, integrated J_{eq} and integrated FAC start to show signatures of enhancements ~ 3 h before t_0, but experience rapid growth in the hour before t_0. The AE index and FAC reach respective maxima of 763 nT and 8.0 MA 40 min after t_0, closely followed by a peak in the integrated westward J_{eq} 58 min after t_0, almost 5 h before the Dst minimum.

Two hours after t_0 the abrupt peak in the integrated FAC quickly decreases to 5.3 MA, before steadily increasing to reach a second maximum of 7.0 MA 5 h and 20 min after t_0, around the time of Dst minimum. In the integrated westward equivalent current the peaks occur 10 - 20 min after the peaks in FACs, but are earlier in the quartiles. This slight difference is likely attributed to changes in the ionospheric Hall conductivity, since the WEJ can be assumed to have the main contribution from Hall currents. The number of substorm onsets peak in the hour before t_0, with an average of 1.25 substorm onsets per hour per storm, indicating high substorm activity and large variability in the electrojets. Newell & Gjerloev (2011b) discussed the distribution of substorms detected by the algorithm and showed that, although 4.4 h was the median separation between substorms, a large number of substorm onsets were identified with less than 1 h separation, as is what we often observe in the storm main phase and particularly around storm onset.

The AL index and the integrated J_{eq} show similarities in the median value, but have vastly different lower quartiles; particularly the last peak in the main phase is far more visible in the quartile of the integrated J_{eq}. This could becomes the spatial coverage of stations that contribute to the AL index is much more limited than that of the SuperMAG network contributing to J_{eq}. In the storm recovery phase the currents and substorm activity level appear to steadily decrease, but even 2.5 days after zero epoch there is still an enhanced activity level compared to quiet time conditions.

Comparing the Dst index, substorm onsets and the integrated FAC and J_{eq}, it is clear that the two steeper slopes in the Dst index during the storm main phase match the times of peak substorm onsets followed by peaks in the integrated FAC and J_{eq}. McPherron et al. (2018) observed large increases in the FAC and SML index following substorm onset, and that substorm onset coincided with the time of largest solar wind-magnetosphere coupling. This agrees with our observations that the largest solar wind driving occurs at the same time as the peak in number of substorm onsets, followed by peaks in the currents. This indicates that the maxima in the ionosphere currents take place during storms and that these times coincide with enhancements in the ring current observed in the Dst index.

The FACs and ionospheric current systems respond and behave differently depending on magnetic local time (MLT). The integrated FACs are divided into four different MLT sectors: noon ($9-15$ MLT), dusk ($15-21$ MLT), midnight ($21-03$ MLT) and dawn ($03-09$ MLT) sector, as shown in Figure 5. The red (blue) line and shading show the superposed value and the upper/lower quartiles of the upward (downward) integrated FAC. Naturally, in dusk (dawn) sector the upward (downward) current is R1 and vice versa for R2. FACs in all of the sectors start increasing slightly before t_0, but the dusk and dawn sectors reach significantly larger peak values than the midnight and noon sectors. This is expected, as the majority of R1 and R2 FACs are concentrated in dusk and dawn. The FAC peak 40 min after t_0 in Figure 4 is seen in all sectors, but the second peak after 5 h and 20 min is only clearly visible in the dusk sector with an earlier second peak seen in the midnight sector. However, in the upper quartiles the second peak is clearly visible in all sectors, and even of larger magnitude than the first in the dusk sector. All in all, the temporal behavior of R1 and R2 currents in different MLT sectors are very similar.

3.2 Effect of solar wind dynamic pressure on FACs and ionospheric currents

To study the difference caused by the SW dynamic pressure in the vicinity of the SIR, the 33 storms were split into groups of low and high p_{dyn}, denoted p^{l}_{dyn} and p^{h}_{dyn} respectively. The division was based on the maximum SW dynamic pressure within ± 3 h from t_0. The median maximum dynamic pressure in all of the events were 6.7 nPa, with a span from the smallest being 2.4 nPa up to 15.7 nPa. As there are an odd number of storms, the p^{l}_{dyn} group contains 16 storms, while the p^{h}_{dyn} group includes the median storm and is therefore made up of 17 storms.

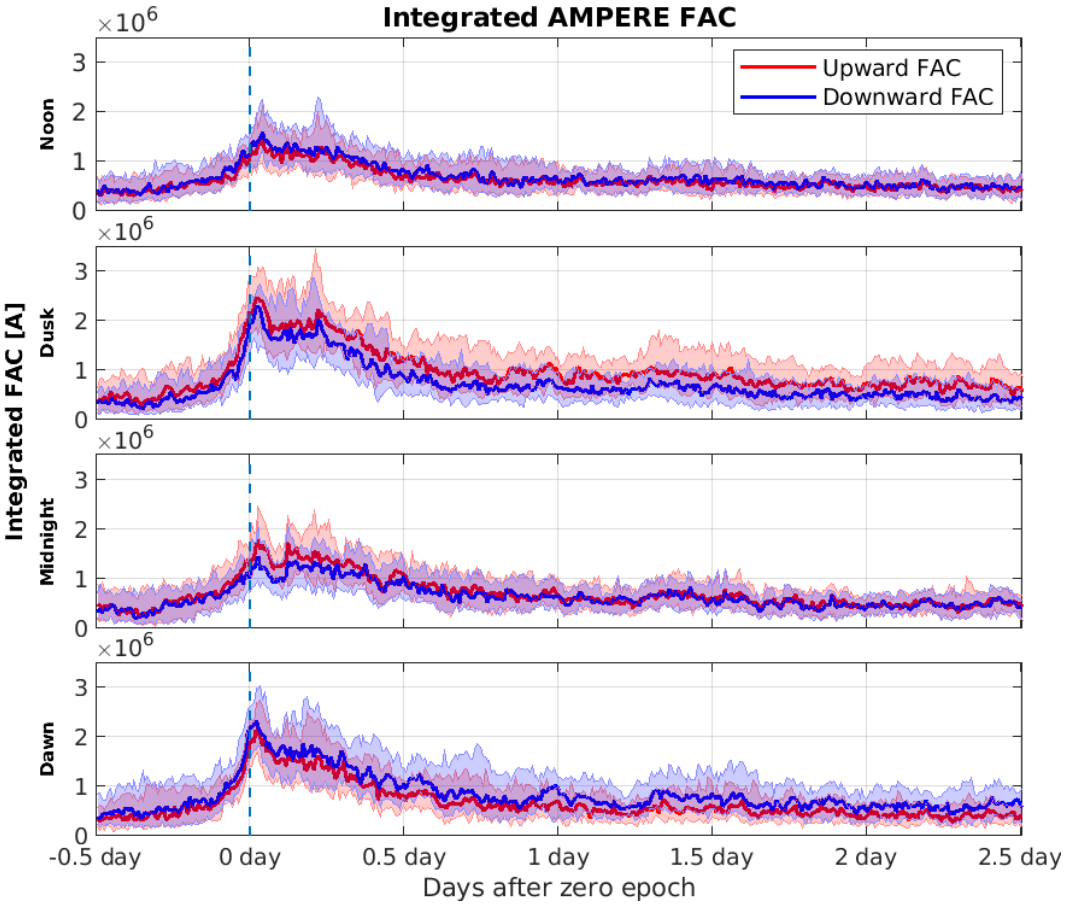

Figure 5: Superposed integrated FAC from AMPERE separated into four different MLT sectors.

Table 2 summarizes the characteristics of the low and high pressure groups. The durations of the main phase in the two categories are very similar and so are the median minimum Dst at −69.5 and −71 nT for the p^{l}_{dyn} and p^{h}_{dyn} storms, respectively. Albeit the similarities, the p^{h}_{dyn} storms are associated with substantially longer storm recovery phases with median of 46.5 h and 85.0 h for p^{l}_{dyn} and p^{h}_{dyn}, respectively, and the three largest events measured by Dst minimum belongs to p^{h}_{dyn} storms.

Figure 6 accompanies Table 2 and shows the distribution of the Dst minimum and the length of the storm main and recovery phase for both the p^{l}_{dyn} and p^{h}_{dyn} storms separately. The top panel of Figure 6 shows a similar number of p^{l}_{dyn} and p^{h}_{dyn} storms in the smallest Dst disturbance intervals from 50-64 nT and 65-79 nT, but the storms where Dst decreases below −95 nT are exclusively p^{h}_{dyn} storms. The middle panel shows the duration of the main phase, where p^{h}_{dyn} storms are slightly favored amongst the storms with the shortest main phase duration. The bottom panel shows the duration of the recovery phase, here p^{l}_{dyn} storms are strongly favored to have short storm recovery phases, while the opposite is the case for p^{h}_{dyn} storms. Seven of the storms have a recovery phase lasting $\geq$ 100 h, of which one is among the p^{l}_{dyn} storms (#28) and six among the p^{h}_{dyn} storms (# 1, 2, 6, 19, 21, and 33). There appears to be no relationship between the length of the recovery phase and the minimum Dst reached.

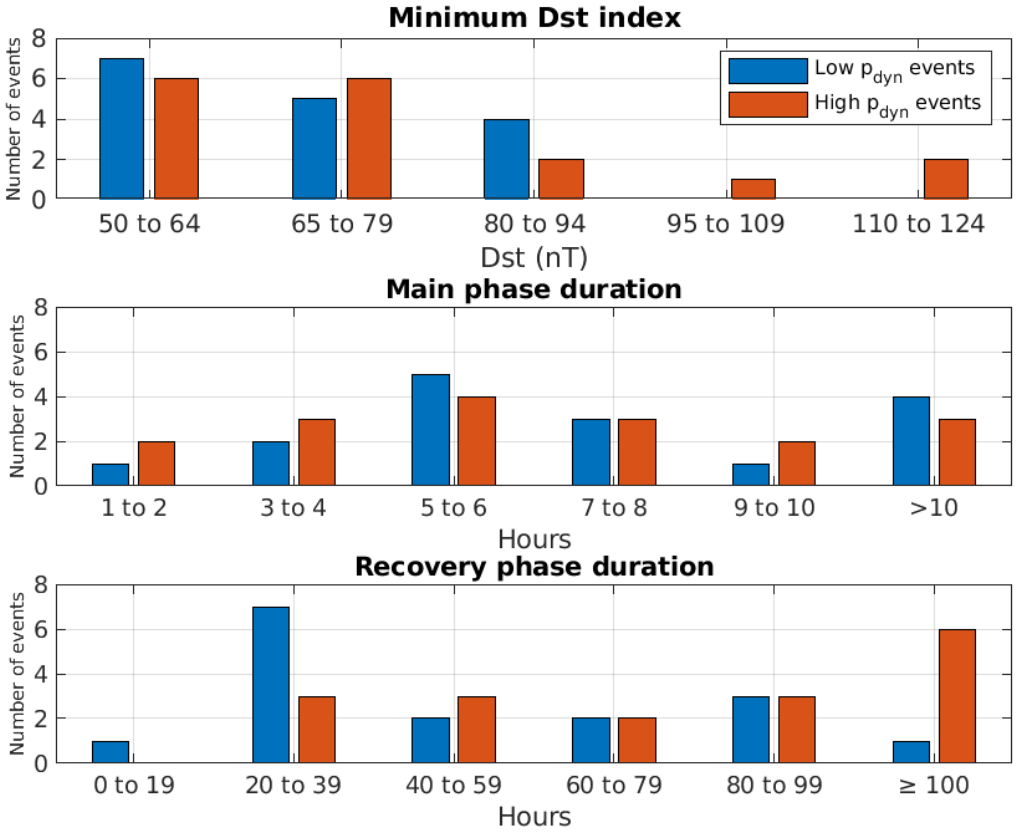

Figure 6: Distribution of minimum Dst and the length of storm main and recovery phase for the low and high p_{dyn} storms.

From inspecting all of the 33 storms individually, none have Dst monotonically relaxing back to quiet time condition in the recovery phase, but all of the storms have some time intervals of further Dst decreases in the recovery phase. What appears to separate the storms with the longest recovery phases from the rest is that the Dst decreases in the recovery phase are larger and more frequent than in the other storms. This could indicate that p^h_{dyn} storms are associated with more frequent and intense injections of particles into the ring current during the recovery phase than p^l_{dyn} storms. However, the Akasofu ε describing solar wind energy input into the magnetosphere is not higher during recovery phase of p^h_{dyn} as will be seen from Figure 7. Alternatively, loss of ring current particles could be more efficient during recovery phases of p^l_{dyn} than p^h_{dyn} storms. Wang et al. (2003) showed that higher dynamic pressure during times of northward IMF orientation decreases the ring current decay time, and as we will see in Figure 7, the p^l_{dyn} storms have a larger dynamic pressure in the storm recovery phase than p^h_{dyn} events.

The IMF and SW conditions for both groups are shown in Figure 7. Two light vertical dashed lines around the zero epoch show the interval used to select the p^l_{dyn} and p^h_{dyn} storms. The top panel shows the SW dynamic pressure where the p^h_{dyn} storms clearly dominate around t_0, but as the pressure in the p^h_{dyn} storms decrease more rapidly because of a much larger SW velocity, creating a greater rarefaction in its wake, the p^l_{dyn} storms have the larger pressure from t_0 + 10 h onwards. Second panel shows the SW flow velocity, which shows that the p^l_{dyn} storms have a more steady and slightly higher flow velocity in

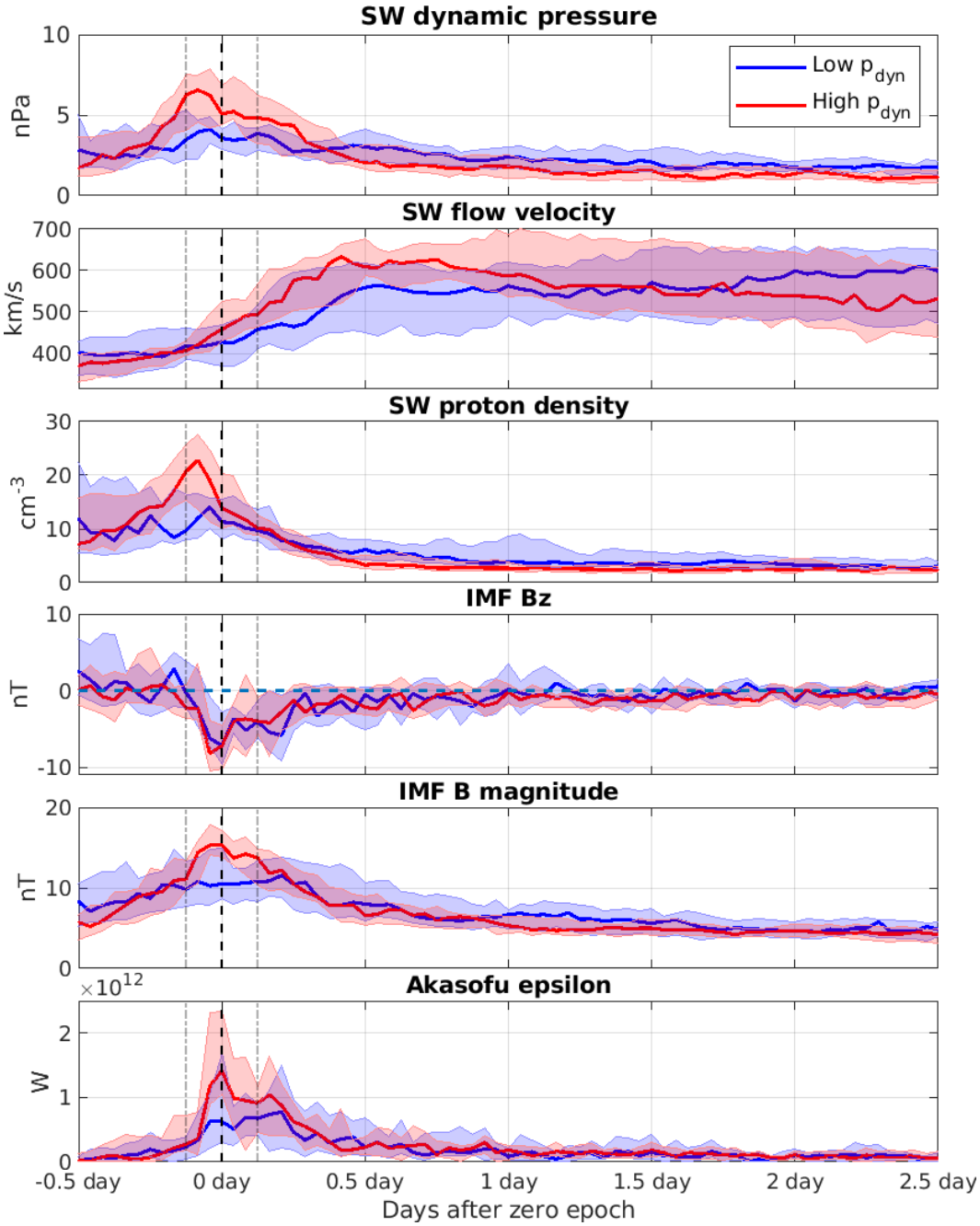

Figure 7: Solar wind parameters and Akasofu ε for the low and high dynamic pressure storms. The blue (red) line is the low (high) pressure category and the shaded area shows the quartiles. The bold dashed vertical line shows the time of zero epoch, and the two faint dashed lines at ±3 h enclose the time interval that the dynamic pressure categories were selected.

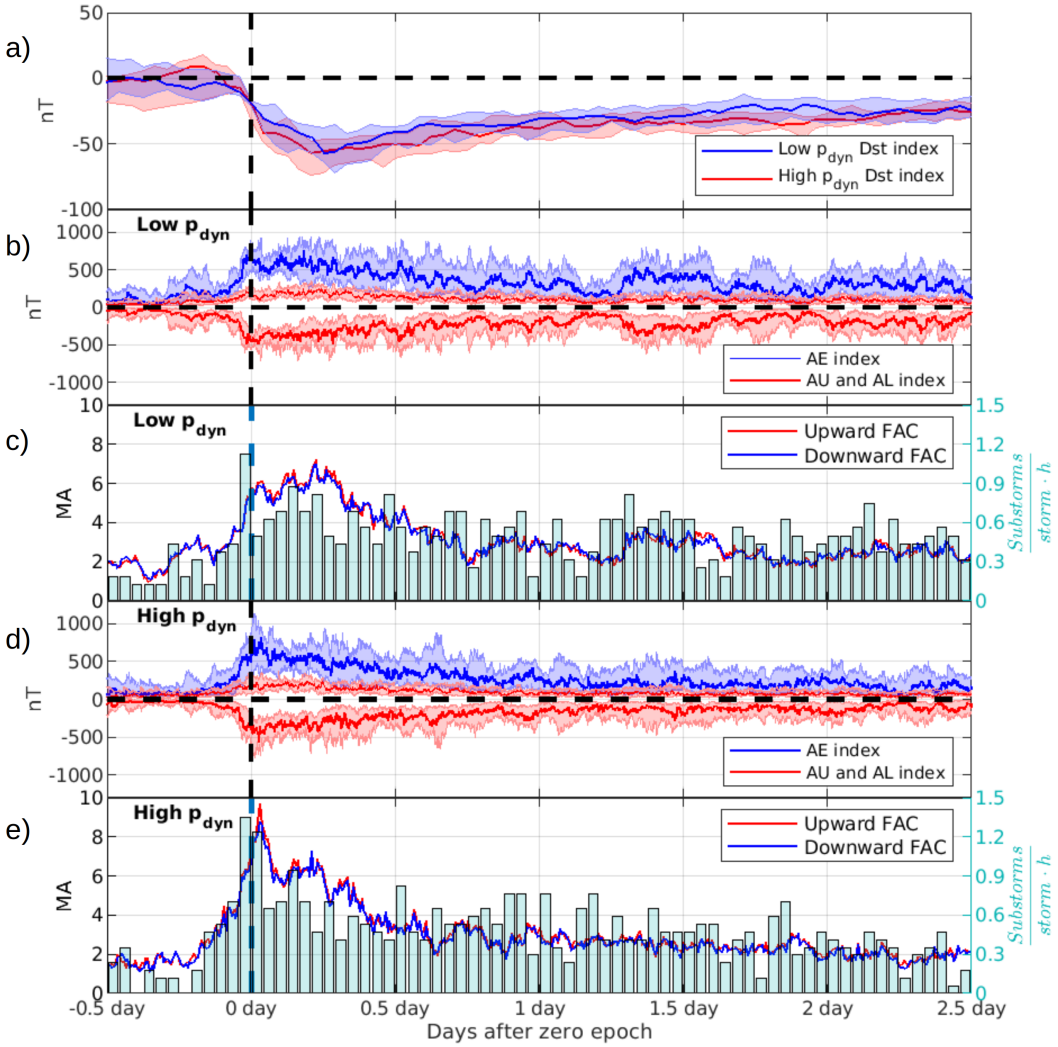

Figure 8: Same as Figure 4, but for low and high dynamic pressure storms.

Table 2: Characteristics of low and high p_{dyn} storms

	Low	High
Number of storms	16	17
Median max p_{dyn}	5.0	8.6
Median min Dst	-70 nT	-71 nT
Min Dst in category	-93 nT	-124 nT
Median main phase duration	6.5 h	6.0 h
Median recovery phase duration	46.5 h	85.0 h
Median storm duration	61.5 h	89.0 h
Median time from HSS onset to t_0	31 h	13 h
Median time from t_0 to max V_{SW}	31 h	18 h

the hours before the t_0. At and after t_0 the flow velocity of p^h_{dyn} storms exceed that in p^l_{dyn} storms, and reaches maximum within the first 12 hours before gradually decreasing. The flow velocity of p^l_{dyn} storms behaves differently, having a much slower increase to maximum, which is not reached within the first 2.5 days after t_0. The third panel shows the SW proton density. Comparing p_{dyn} to SW velocity and density shows that the largest contribution to p_{dyn} around the time of t_0 comes from the density, although the higher flow velocity in the p^h_{dyn} storms are likely indirectly responsible for this difference in the proton density at the front of the SIRs. From t_0 + 10 h onwards the p^l_{dyn} storms have a larger proton density than the p^h_{dyn} storms. The fourth panel shows the B_Z component of the IMF. B_Z behaves very similarly in both categories, both in terms of timing, magnitude and variability. This is likely because it is one of the main factors that makes the HSS/SIR geoeffective, and any moderate or large storm (Dst ≤ -50 nT) requires a substantially negative B_Z component. The second last panel shows the IMF magnitude, B. As with the SW density, the IMF magnitude is substantially larger in the p^h_{dyn} cases compared to the p^l_{dyn} around the onset of the storm. This is also a signature of the compression of plasma and magnetic field lines in the SIR portion of the HSS. Last panel shows the Akasofu coupling function which indicates a larger SW-magnetosphere coupling for the p^h_{dyn} storms compared to the p^l_{dyn} storms in the storm main phase. In both groups the upper quartile shows two peaks in coupling, one at t_0 and another (smaller in the case of high p_{dyn}) roughly 4 to 5 hours later, with the p^h_{dyn} having larger energy transfer than p^l_{dyn} in both peaks.

Figure 8 shows the superposed Dst index, AE, AU and AL indices, and the integrated FAC with number of substorm onsets for the p^l_{dyn} and p^h_{dyn} storms, respectively. The Dst index of the p^h_{dyn} storms show a slight positive excursion three to six hours before t_0, which is an indication of storm sudden commencement (SSC) (see e.g. Joselyn & Tsurutani, 1990). This feature is not visible in the p^l_{dyn} storms or in Figure 4 where all storms were superposed. Following the onset we see that the superposed Dst index reaches minimum around the same time, 6 and 5 hours after t_0 for p^l_{dyn} and p^h_{dyn}, respectively. However, the p^h_{dyn} storms have a steeper decrease in Dst immediately after t_0, that also corresponds to a large increase and maximum in both the AE index and integrated FAC seen in panel d) and e). The largest difference between the p^l_{dyn} and p^h_{dyn} storms occurs in the hours before t_0 and until 2 hours afterwards. During this period both the AE indices and the integrated FAC in the p^h_{dyn} storms are clearly larger and develop faster than the p^l_{dyn} storms. The first peak seen in the FAC of Figure 4 is in the p^h_{dyn} storms at t_0 + 40 min. The p^l_{dyn} storms reach maximum FAC at t_0 + 5 h and 20 min. The p^l_{dyn} storms do not reach one outstanding maximum AE peak as the p^h_{dyn} storms do, but instead have an enhanced value fluctuating around 700 nT for the first 6 hours after t_0. From t_0 + 5h and 20 min, at the time of (the second)

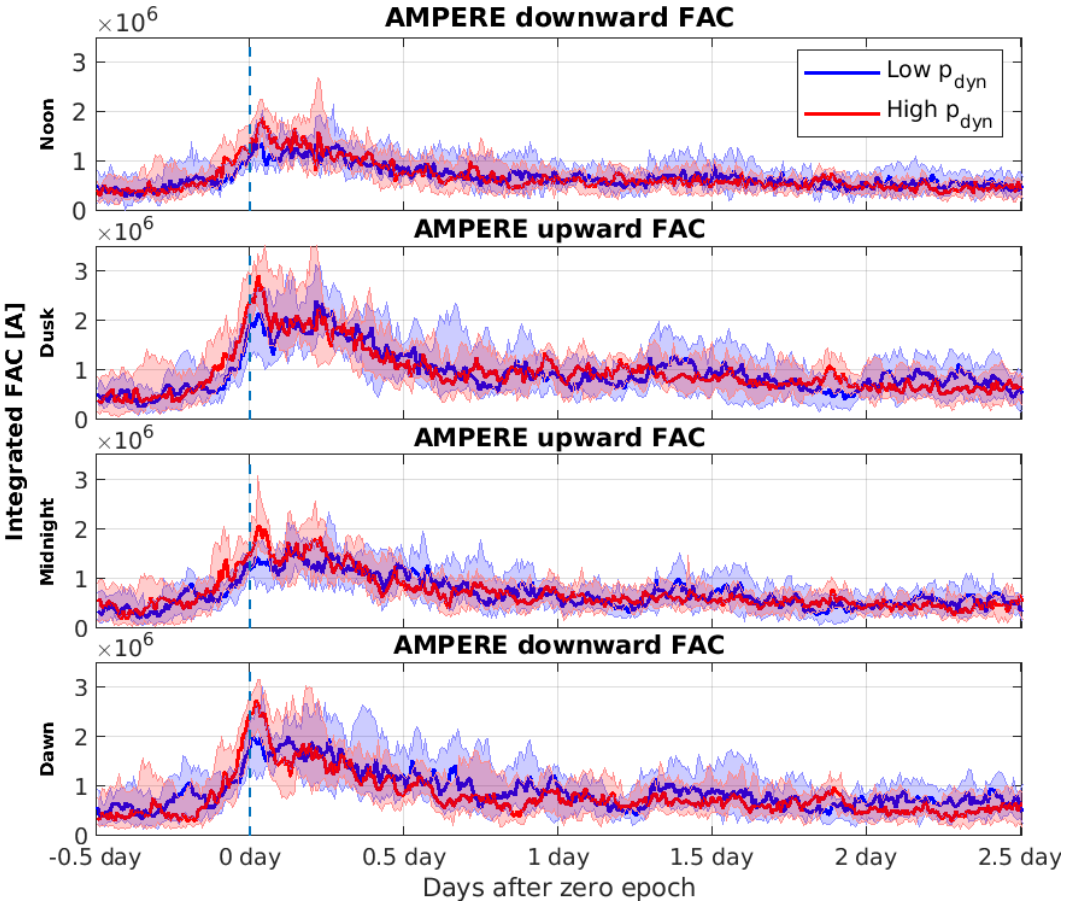

Figure 9: Integrated dominant (Region 1) FAC in four MLT sectors for low and high p_{dyn}, i.e. for the dusk and midnight sectors the upward current is shown, and for the noon and dawn sectors the downward current is shown.

FAC peak and around the time of Dst minimum, the FACs of both p^{l}_{dyn} and p^{h}_{dyn} storms start steadily decreasing for the next 12 h until reaching a lower but still enhanced state where it remain for several days. The number of substorm onsets in Figure 4 for all the 33 storms maximized in the hour before and after t_0, but in Figure 8 it is evident that this only resemble the p^{h}_{dyn} storms. The p^{l}_{dyn} storms also have increased numbers of substorm onsets in the hour before t_0, but a large drop in the hour after t_0 that agrees with the lower FAC and horizontal equivalent current (will be seen in Figure 10) activity compared to the p^{h}_{dyn} storms.

Figure 9 shows the integrated FAC split into four different MLT sectors. This is similar to Figure 5, but for p^{l}_{dyn} and p^{h}_{dyn} storms and with only the dominant R1 oriented current shown in each panel. These currents consist of the R1 FACs mapping to the magnetopause and possibly also the FACs in the substorm current wedge mapping to the magnetotail. The most pronounced difference in the FAC for these two categories occurs during the first hour after onset, when the FACs in p^{h}_{dyn} events reaches a prominent peak that is not seen in the p^{l}_{dyn} events. In all sectors the currents in the p^{h}_{dyn} storms reach maximum in the hour following t_0 and then rapidly decrease by 30% to 40% within the next hour. From then on the currents stabilize and in all sectors except for noon show tendencies to slightly increase throughout the remaining of the main phase. Meanwhile, the p^{l}_{dyn} storms have a sharp increase in both dusk and dawn sectors at the time of t_0, but contrary to p^{h}_{dyn} storms,

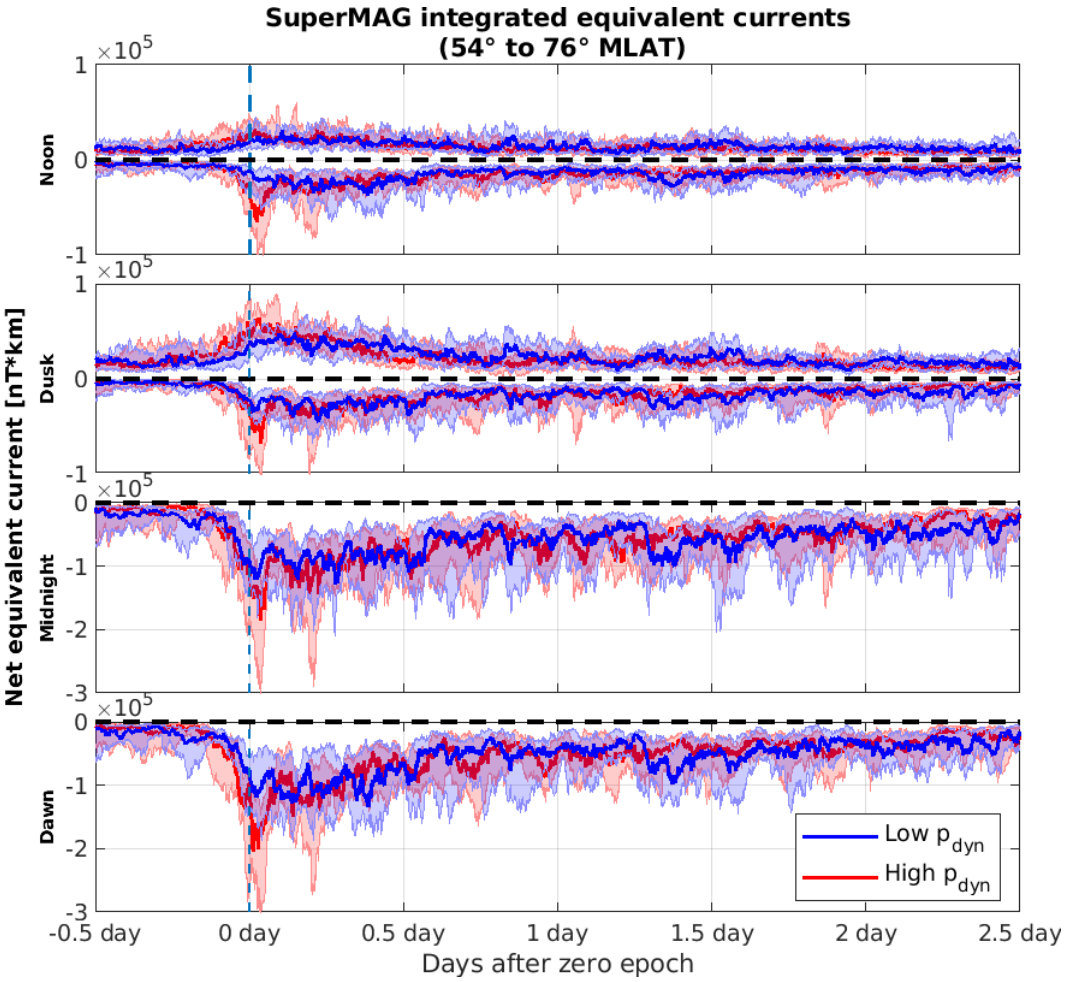

Figure 10: SuperMAG integrated equivalent currents in four different MLT sectors. In the two top panel, noon and dusk sectors, both the EEJ and WEJ are shown. In the two bottom panels only the WEJ is shown as the eastward portion of the current in these sectors is negligible.

the currents do not reach an outstanding maximum, but remain at a steady level for 5 h before reducing similarly as the p^{h}_{dyn} in the storm recovery phase. The p^{h}_{dyn} storms shows signature of a second FAC maximum in the upper quartile in all sectors, but largest spikes in the dusk and noon sectors 5 h after t_0.

The equivalent currents shown in Figure 10 are integrated from the SuperMAG data spanning magnetic latitudes from 54° to 76°. The first two panels show the noon and dusk sectors, respectively, and contain the EEJ and WEJ. The last two panels show the midnight and dawn sectors, respectively, and only include the WEJ, as the EEJ is very small in these sectors. During the quiet hours before the onset both p^{l}_{dyn} and p^{h}_{dyn} storms have little activity, but in the three hours leading up to the storm onset the currents in the p^{h}_{dyn} storms start increasing faster than the p^{l}_{dyn} storms. This is particularly seen in the lower quartile of the WEJ. Two maxima can be seen in the p^{h}_{dyn} storms in the lower quartiles, closely matching the times of the upper quartile peaks in the FAC in Figure 9, one at t_0 + 51 min and one at t_0 + 5h. In all sectors the peak in median and upper quartile of the p^{h}_{dyn} storms integrated equivalent current seem to match a peak in the integrated FAC by at most 30 min separation.

3.3 Solar wind-magnetosphere coupling, integrated FAC and AE index

Table 3: Correlation coefficients between Akasofu ε, AE and integrated FAC for the three groups (all storms, high p_{dyn} storms and low p_{dyn} storms) shown in Figure 11.

	All	Low	High
r(ε, AE)	0.79	0.70	0.83
r(ε,FAC)	0.89	0.88	0.92
r(AE,FAC)	0.91	0.88	0.93

In order to study how well the currents are predicted by the solar wind, the superposed 1 h averaged Akasofu ε, integrated FAC and AE index are shown in Figure 11. The top panel shows all events together, the middle panel high pressure storms and the bottom panel low pressure storms. The temporal evolution of the integrated FAC and AE index follow the behaviour of the Akasofu ε very closely in all three panels, indicating that the magnetosphere-ionosphere coupling during this period is to a large extent directly driven by the solar wind. Akasofu ε has a rapid increase starting 2 h before t_0 for all storms and the high pressure storms, and it precedes the integrated FAC and AE index by reaching maximum 1 h earlier. After the storm main phase ends, ε drops off faster than the FAC and AE index. The FAC and AE index follow closely each other and reach maxima of equal relative magnitude in all three panels.

Even though the temporal behaviour of Akasofu ε and the currents are similar in Figure 11, the scaling factors between the low and high pressure storms are different, since for p^{h}_{dyn} storms the peak Akasofu ε is 1.42 TW and the peak FAC is 9.2 MA, while for p^{h}_{dyn} storms the corresponding figures are 0.77 TW and 7.0 MA.

All storms (top panel) show both of the peaks like the high p_{dyn} storms. In a previous section, we showed that also equivalent currents show these two peaks: one near the onset of the HSS/SIR-driven storm and the other about 5 h later. The superposed Dst index decreases in two intervals that both coincide with the times of largest increase in the currents leading to the two peaks. Yokoyama & Kamide (1997) and Kamide, Yokoyama, et al. (1998) also observed a two-peak structure in the energy injection to the ring current, in the IMF B_Z and in the AE indices during the main phase of moderate and intense storms. They

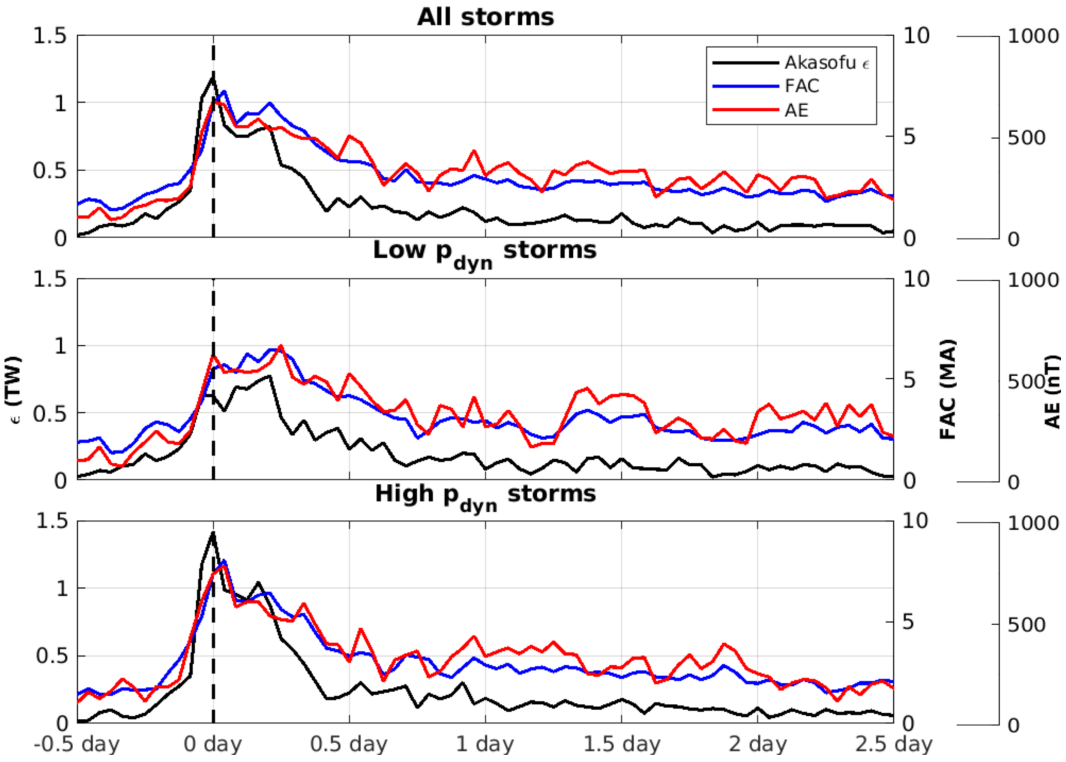

Figure 11: One hour averaged Akasofu ϵ, total integrated FAC and AE index are plotted for all, low and high p_{dyn} storms.

suggested as one possible explanation that these features were associated with ICMEs, and that the first peak occurring around the storm onset would be related to a compressed southward oriented IMF (sheaths) and that the second peak just before Dst minimum was caused by the southward IMF portion of the main ejecta or magnetic cloud. The storms in this study are associated with HSS/SIR events and it is shown that the peaks are directly driven by the solar wind coupling. The first peak in the Akasofu ε shortly after t_0 is driven by large compression in the SW IMF accompanied by southward B_Z, but the main driver of the 2nd peak is not quite as obvious. By studying each term in the Akasofu ε individually (plots not shown), the second peak seems to be driven by a combination of compressed IMF and spikes in the $\sin(\theta/2)^4$ term.

Table 3 shows the Pearson correlation coefficients in Figure 11 for all, low and high p_{dyn} storms presented. The highest correlation is found between AE and FAC in all the groups, varying between 0.88 and 0.93. This is natural, because both parameters are related to currents in the ionosphere. However, correlation between Akasofu ε and FAC is almost as high, for all events 0.89 and for high p_{dyn} storms even 0.92. Correlation between Akasofu ε and AE is clearly smaller, though still high, for all events 0.79 and for high p_{dyn} storms 0.83. The correlations are higher for p^h_{dyn} storms than for the p^l_{dyn} storms. The correlation between Akasofu ε and AE estimated by Newell et al. (2008) was 0.67, which is smaller than our 0.79 for all HSS/SIR events. This is understandable, because Newell was not focused on HSS/SIR storms, but included all solar wind conditions. Another difference between our study and Newell et al. (2008) is that we have made the correlation analysis using superposed data. High correlation between the AE indices and the FACs have also been reported previously, e.g. Coxon et al. (2014a) found that correlation coefficient between the R1 FAC and AL index was -0.83 and between the R2 FAC and AL index of -0.79.

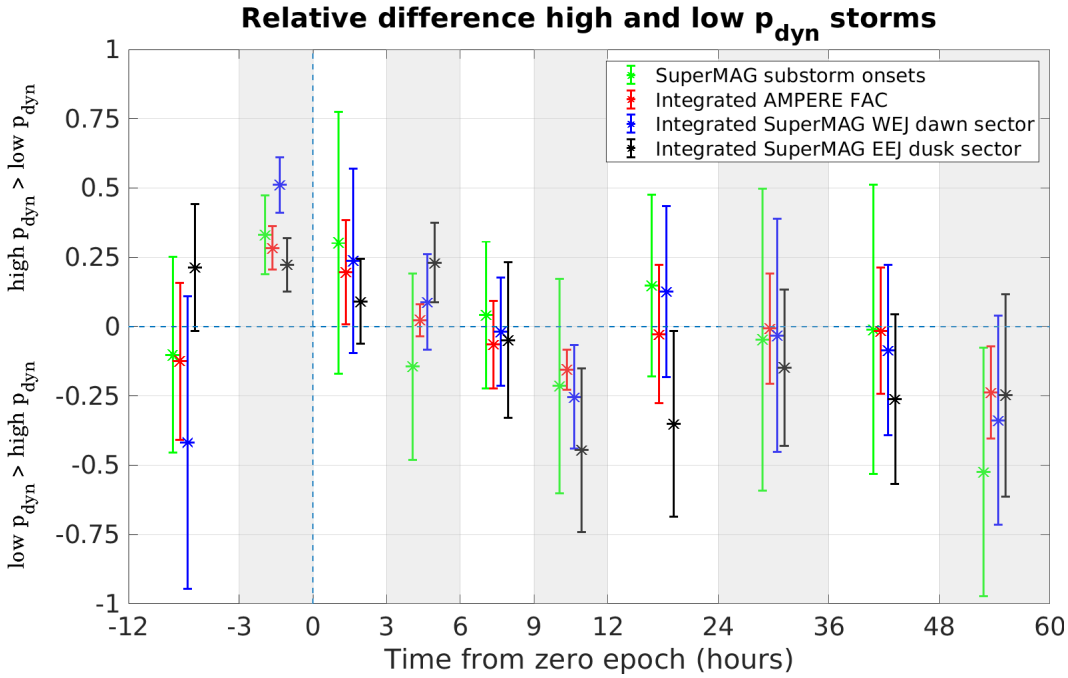

Figure 12: Relative difference between high and low p_{dyn} events for the data sets averaged over the white/grey shaded intervals - i.e. 9 h for the first interval containing the pre-onset conditions with the lowest activity, 3 h intervals from -3 h until 12 h after t_0. From 12 to 60 h after t_0 the average relative difference is calculated over 12 h intervals.

4 Discussion

In the earlier sections, the storms were divided into two categories based on the dynamic pressure in the vicinity of the SIR. Here the differences are further elaborated. Figure 12 is a summary of the relative difference between the p^h_{dyn} and p^l_{dyn} storms. The AMPERE FAC and SuperMAG equivalent currents are averaged into 30 min bins before calculating the relative difference:

$$\mu = \frac{1}{N}\sum_{i=1}^{N}\frac{x_i^h - x_i^l}{\frac{1}{2}\left(x_i^h + x_i^l\right)} \tag{7}$$

and standard deviation as:

$$\sigma = \sqrt{\frac{1}{N}\sum_{i=1}^{N}\left(\frac{x_i^h - x_i^l}{\frac{1}{2}\left(x_i^h + x_i^l\right)} - \mu\right)^2}. \tag{8}$$

Here x^l and x^h are the data sets (number of substorm onsets, integrated FAC and integrated SuperMAG EEJ and WEJ currents) for low and high dynamic pressure storms, respectively. The calculation is done over all the averaged data points N within each time interval. The duration of the time intervals are 3 h, except 9 h well before the storm [t_0-12h, t_0-3h] (read as "from t_0 - 12 h to t_0 - 3 h") and 12 h in the late recovery phase from t_0 + 12h onwards.

The difference imposed by the high and low p_{dyn} condition is primarily seen in the interval [t_0-3h, t_0+3h], with less difference in the recovery phase of the storm. Larger p_{dyn} at the onset of the storm appear to induce a stronger magnetospheric response and more rapid growth in the FAC and equivalent current system along with more substorm onsets. Comparing the time intervals [t_0-3h, t_0] and [t_0, t_0+3h] in Figures 12 and 7, it is clear that the larger intensity of the high p_{dyn} storms at this time coincides with increased solar wind driving. In the interval spanning [t_0+3h, t_0+9h], covering the time of Dst minimum and the second peak in the integrated FAC and equivalent currents, there is no significant difference between the pressure categories. However, during [t_0+9h, t_0+12h] there is a reversed situation where the FAC, equivalent currents and substorm activity are all larger in the low dynamic pressure storms. In the recovery phase [t_0+12h, t_0+48h] both groups behave similarly, but in the last interval from [t_0+48h, t_0+60h] the low pressure storms have again significantly more ionospheric activity than the high pressure storms. The only SW parameter that differs between the two groups at this time interval is the SW flow velocity, with the low pressure storms having larger values (Figure 7, second panel).

Liu et al. (2019) found that the impact of SW p_{dyn} and E_Y on the mid/low latitude ground magnetic perturbation ΔH were largest on the dayside during the storm initial phase due to the compression of the magnetopause and enhancement of the Chapman-Ferraro current. In the main phase the ΔH in all MLT sectors decreased, but with peaks in the dusk sector and can explain the large westward equivalent currents we observe at mid latitudes in Figure 3 after t_0. Le et al. (2020) showed that p_{dyn} plays a crucial role in the intensity of major geomagnetic storms, and they argued that large and long lasting southward IMF may alone not be sufficient if p_{dyn} is much lower than 3 nPa. In our study the value dividing low and high pressure storms was 6.7 nPa.

The main focus of previous research relating the SW p_{dyn} to the magnetosphere-ionosphere system has been on the low/mid-latitude region as the magnetic signatures there are directly influenced by the Chapman-Ferraro and ring current. However, the R1 FACs close partially through the Chapman-Ferraro current and the R2 FACs through the ring current and are therefore closely connected to changes happening in these systems (Iijima et al., 1990; Tsyganenko & Stern, 1996). Palmroth et al. (2004) found significant correlation between increases in the SW p_{dyn} and ionospheric Joule heating at high latitudes, and noted that the AE index increased by 35% 20 min after a pressure pulse during southward IMF. This is of similar size to the changes that are seen in the AE index, integrated FACs and equivalent currents between the high and low p_{dyn} events. The largest impact of the dynamic pressure on the ionospheric currents occur in the beginning of the storm main phase around the time of t_0. This is earlier than what was reported by Nakano et al. (2009), who found high correlation between the p_{dyn} and R2 FAC during storm times when the ring current was strongly enhanced. They speculated that the plasma pressure in the ring current played a crucial part of the effect the SW p_{dyn} has on the magnetosphere and R2 currents.

From the SW and IMF data it is clear that the largest contribution to the dynamic pressure comes from the SW density. This is expected as the majority of the HSS/SIR storms develop in the SIR at the interface between the slow and high SW. Weigel (2010) found by studying the evolution of the Dst index that the SW density modifies the solar wind's geoefficiency to a greater degree than p_{dyn}, and that the influence on the geoefficiency from increased SW density was smaller for larger storms. This agrees with our observations as both p^{l}_{dyn} and p^{h}_{dyn} storms reach similar median Dst minima. It appears that p_{dyn} has more profound impact on the way the storm develops and on the magnitude of auroral currents during the first hour after storm onset.

5 Summary and conclusions

In this study, FACs and ionospheric equivalent currents in HSS/SIR driven storms have been analysed using AMPERE and SuperMAG data. To be included, storms had to reach at least -50 nT and occur during a HSS/SIR event listed by Grandin et al. (2019). In total, 51 HSS/SIR driven storms were detected during the years $2010 - 2017$, with full data coverage available for 33 storms, which were selected for this study (Table 2). To our knowledge, this is the first statistical superposed epoch analysis (SEA) study of global FACs and horizontal currents behaviour during HSS/SIR-driven storms.

The storms were analyzed using SEA with zero epoch (t_0) centered at the onset of the main phase, which was in this study defined as the time when the Dst index decreased below -15 nT. The evolution and distribution of FACs and horizontal equivalent currents in the entire high latitude ($\geq 40°$ MLAT) northern hemisphere have been studied. The storms were also separated into low and high dynamic pressure events, denoted p^{l}_{dyn} and p^{h}_{dyn}, respectively, based on the solar wind dynamic pressure values within ± 3 h of t_0. When looking at solar wind parameters, this time interval roughly corresponds to the SIR portion of the HSS, containing compressed solar wind plasma ahead of the high-speed flows.

The main findings are:

- Moderate to strong HSS/SIR storms tend to begin when the SIR with enhanced solar wind density and compressed magnetic field with B_Z pointing in the southward direction is interacting with the magnetopause.
- For high p_{dyn} events, the solar wind velocity maximum is reached earlier than for low p_{dyn} events. Also, the lead times to storm onset is shorter for high than low p_{dyn} events (13 h and 31 h, respectively).
- The superposed Dst minimum for all the storms is -56 nT and occurs 6 h after the storm onset time. When separated into p^{l}_{dyn} and p^{h}_{dyn} storms, no significant difference is found between the superposed minimum Dst value and the main phase duration.
- However, typically only the p^{h}_{dyn} events show a signature of a SSC before the storm onset, have profoundly longer storm recovery phase duration (85 h and 46.5 h for p^{h}_{dyn} and p^{l}_{dyn} storms, respectively) and contain the three largest events measured by minimum Dst.
- The integrated currents have two peaks in the main phase. In the upward and downward FACs, the first peak of 8.0 MA takes place 40 min after t_0 and a less intense, but broader peak of 7.0 MA occurs 5 h and 20 min after t_0, in the end of the main phase. At the same times, also the equivalent currents peak.
- The first peak in the currents is associated with p^{h}_{dyn} storms and in that category the maximum FAC is 9.2 MA. The second peak in the end of the storm main phase is observed both for p^{l}_{dyn} and p^{h}_{dyn} storms and is the largest peak for p^{l}_{dyn} storms and the second largest peak for p^{h}_{dyn} storms, in both cases reaching a value 7.0 MA.
- Substorm onsets peak one hour before t_0 for both p^{l}_{dyn} and p^{h}_{dyn} storms. Since t_0 is the time when Dst has dropped below -15 nT, this indicates that substorms commence at about the same time as the storm starts to develop. A second peak in the number of substorm onsets (1-h resolution data) is seen in the hour before the second peak in the integrated currents for both p^{l}_{dyn} and p^{h}_{dyn} storms.
- In the main phase the Dst index decreases in two intervals at the same time as the number of substorm onsets peak and currents are increasing towards their peak values. Hence, it appears that particle injections into the ring current take place in association with substorm onsets and intensifications of the ionospheric R1/R2 current systems. It is assumed that also substorm current wedges are formed, but it is not possible to extract those from the spatially and temporally superposed data.
- The temporal evolution of HSS/SIR-driven storms is very strongly driven by the solar wind. The Akasofu ε parameter (1-h resolution) has a similar temporal behaviour as the FACs have for both p^{l}_{dyn} and p^{h}_{dyn} events. The SW-magnetosphere coupling is

considerably larger for high than low p_{dyn} storms in the main phase (peak values 1.42 TW and 0.77 TW, respectively). For p^{h}_{dyn} storms, Akasofu ε peaks at storm onset, while for p^{l}_{dyn} storms the peak occurs 5 h after onset.

- In the storm recovery phase, Akasofu ε decreases to pre-storm time conditions, but the currents as well as the number of substorm onsets still remain high, and higher for p^{l}_{dyn} than p^{h}_{dyn} storms. After about 2 days from the storm onset, the number of substorm onsets becomes clearly higher for low than high p_{dyn} events. At this time, solar wind velocity and the dynamic pressure become higher for p^{l}_{dyn} than p^{h}_{dyn} events, indicating that solar wind velocity in the recovery phase may play an important role in substorm generation.
- The strong driving of the ionosphere by the solar wind is also evidenced by the high correlation coefficient between the Akasofu ε and FAC, which is 0.89, and between Akasofu ε and AE, 0.79. Not surprisingly, the correlation coefficient between the ionospheric parameters AE and FAC is very high, 0.91.
- All the correlation coefficients are higher for the superposed p^{h}_{dyn} storms than for the superposed p^{l}_{dyn} storms. This is likely due to the fact that p^{h}_{dyn} storms have significantly higher Akasofu ε values than p^{l}_{dyn} during the storm main phase. The correlation coefficient between the Akasofu ε and FAC is 0.92 for p^{h}_{dyn} storms.

Acknowledgments

This work was supported by the Academy of Finland project 314664 and 314670. We thank the AMPERE team and the AMPERE Science Center for providing the Iridium derived data products (http://ampere.jhuapl.edu/index.html). For the ground magnetometer data and substorm onset list we gratefully thank the SuperMAG collaboration and all organizations involved (https://supermag.jhuapl.edu/info/). For the geomagnetic indices, solar wind and interplanetary magnetic field data we gratefully thank NASA/GSFC's Space Physics Data Facility's OMNIWeb (https://omniweb.gsfc.nasa.gov/). All data used in this study can be accessed through the links given above. We would also like to thank Ari Viljanen for insightful discussions and constructive comments on the manuscript.

References

Akasofu, S.-I. (1981). Energy coupling between the solar wind and the magnetosphere. *Space Science Reviews*, *28*(2), 121–190. doi: https://doi.org/10.1007/BF00218810

Anderson, B., Korth, H., Waters, C., Green, D., Merkin, V., Barnes, R., & Dyrud, L. (2014). Development of large-scale birkeland currents determined from the active magnetosphere and planetary electrodynamics response experiment. *Geophysical Research Letters*, *41*(9), 3017–3025. doi: https://doi.org/10.1002/2014GL059941

Anderson, B., Korth, H., Waters, C., Green, D., & Stauning, P. (2008). Statistical birkeland current distributions from magnetic field observations by the iridium constellation. In *Annales geophysicae* (Vol. 26, pp. 671–687). doi: https://doi.org/10.5194/angeo-26-671-2008

Anderson, B., Ohtani, S.-I., Korth, H., & Ukhorskiy, A. (2005). Storm time dawn-dusk asymmetry of the large-scale birkeland currents. *Journal of Geophysical Research: Space Physics*, *110*(A12). doi: https://doi.org/10.1029/2005JA011246

Anderson, B., Takahashi, K., Kamei, T., Waters, C., & Toth, B. (2002). Birkeland current system key parameters derived from iridium observations: Method and initial validation results. *Journal of Geophysical Research: Space Physics*, *107*(A6), SMP–11. doi: https://doi.org/10.1029/2001JA000080

Anderson, B., Takahashi, K., & Toth, B. A. (2000). Sensing global birkeland currents with iridium® engineering magnetometer data. *Geophysical Research Letters*, *27*(24), 4045–4048. doi: https://doi.org/10.1029/2000GL000094

Baker, K., & Wing, S. (1989). A new magnetic coordinate system for conjugate studies at

high latitudes. *Journal of Geophysical Research: Space Physics*, *94*(A7), 9139–9143. doi: https://doi.org/10.1029/JA094iA07p09139

Balogh, A., Gosling, J., Jokipii, J., Kallenbach, R., & Kunow, H. (1999). *Corotating interaction regions* (Vol. 7). Springer Science & Business Media.

Belcher, J., & Davis Jr, L. (1971). Large-amplitude alfvén waves in the interplanetary medium, 2. *Journal of Geophysical Research*, *76*(16), 3534–3563. doi: https://doi.org/10.1029/JA076i016p03534

Borovsky, J. E., & Denton, M. H. (2006). Differences between cme-driven storms and cir-driven storms. *Journal of Geophysical Research: Space Physics*, *111*(A7). doi: https://doi.org/10.1029/2005JA011447

Boudouridis, A., Zesta, E., Lyons, L., Anderson, P., & Lummerzheim, D. (2004). Magnetospheric reconnection driven by solar wind pressure fronts. doi: https://doi.org/10.5194/angeo-22-1367-2004

Boudouridis, A., Zesta, E., Lyons, L., Anderson, P., & Lummerzheim, D. (2005). Enhanced solar wind geoeffectiveness after a sudden increase in dynamic pressure during southward imf orientation. *Journal of Geophysical Research: Space Physics*, *110*(A5). doi: https://doi.org/10.1029/2004JA010704

Boudouridis, A., Zesta, E., Lyons, R., Anderson, P., & Lummerzheim, D. (2003). Effect of solar wind pressure pulses on the size and strength of the auroral oval. *Journal of Geophysical Research: Space Physics*, *108*(A4). doi: https://doi.org/10.1029/2002JA009373

Burns, A., Solomon, S., Qian, L., Wang, W., Emery, B., Wiltberger, M., & Weimer, D. (2012). The effects of corotating interaction region/high speed stream storms on the thermosphere and ionosphere during the last solar minimum. *Journal of atmospheric and solar-terrestrial physics*, *83*, 79–87. doi: https://doi.org/10.1016/j.jastp.2012.02.006

Cliver, E., Kamide, Y., & Ling, A. (2000). Mountains versus valleys: Semiannual variation of geomagnetic activity. *Journal of Geophysical Research: Space Physics*, *105*(A2), 2413–2424. doi: https://doi.org/10.1029/1999JA900439

Coxon, J., Milan, S., Clausen, L., Anderson, B., & Korth, H. (2014b). A superposed epoch analysis of the regions 1 and 2 birkeland currents observed by ampere during substorms. *Journal of Geophysical Research: Space Physics*, *119*(12), 9834–9846. doi: https://doi.org/10.1002/2014JA020500

Coxon, J., Milan, S. E., Clausen, L. B. N., Anderson, B. J., & Korth, H. (2014a). The magnitudes of the regions 1 and 2 birkeland currents observed by ampere and their role in solar wind-magnetosphere-ionosphere coupling. *Journal of Geophysical Research: Space Physics*, *119*(12), 9804-9815. doi: https://doi.org/10.1002/2014JA020138

Dungey, J. W. (1961). Interplanetary magnetic field and the auroral zones. *Physical Review Letters*, *6*(2), 47. doi: https://doi.org/10.1103/PhysRevLett.6.47

Gjerloev, J. (2009). A global ground-based magnetometer initiative. *Eos, Transactions American Geophysical Union*, *90*(27), 230–231. doi: https://doi.org/10.1029/2009EO270002

Gjerloev, J. (2012). The supermag data processing technique. *Journal of Geophysical Research: Space Physics*, *117*(A9). doi: https://doi.org/10.1029/2012JA017683

Gjerloev, J., & Hoffman, R. (2014). The large-scale current system during auroral substorms. *Journal of Geophysical Research: Space Physics*, *119*(6), 4591–4606. doi: https://doi.org/10.1002/2013JA019176

Gonzalez, W. D., Joselyn, J. A., Kamide, Y., Kroehl, H. W., Rostoker, G., Tsurutani, B. T., & Vasyliunas, V. M. (1994). What is a geomagnetic storm? *Journal of Geophysical Research: Space Physics*, *99*(A4), 5771-5792. doi: 10.1029/93JA02867

Gonzalez, W. D., Tsurutani, B. T., & De Gonzalez, A. L. C. (1999). Interplanetary origin of geomagnetic storms. *Space Science Reviews*, *88*(3-4), 529–562. doi: https://doi.org/10.1023/A:1005160129098

Gosling, J. T., Asbridge, J., Bame, S., & Feldman, W. (1978). Solar wind stream interfaces. *Journal of Geophysical Research: Space Physics*, *83*(A4), 1401–1412. doi: https://doi.org/10.1029/JA083iA04p01401

Grandin, M., Aikio, A. T., & Kozlovsky, A. (2019). Properties and geoeffectiveness of solar wind high-speed streams and stream interaction regions during solar cycles 23 and 24. *Journal of Geophysical Research: Space Physics*, *124*(6), 3871–3892. doi: https://doi.org/10.1029/2018JA026396

Haaland, S., & Gjerloev, J. (2013). On the relation between asymmetries in the ring current and magnetopause current. *Journal of Geophysical Research: Space Physics*, *118*(12), 7593-7604. doi: 10.1002/2013JA019345

Iijima, T., Potemra, T., & Zanetti, L. (1990). Large-scale characteristics of magnetospheric equatorial currents. *Journal of Geophysical Research: Space Physics*, *95*(A2), 991–999. doi: https://doi.org/10.1029/JA095iA02p00991

Iijima, T., & Potemra, T. A. (1978). Large-scale characteristics of field-aligned currents associated with substorms. *Journal of Geophysical Research: Space Physics*, *83*(A2), 599–615. doi: https://doi.org/10.1029/JA083iA02p00599

Ilie, R., Liemohn, M. W., Thomsen, M. F., Borovsky, J. E., & Zhang, J. (2008). Influence of epoch time selection on the results of superposed epoch analysis using ace and mpa data. *Journal of Geophysical Research: Space Physics*, *113*(A3). doi: https://doi.org/10.1029/2008JA013241

Jian, L., Russell, C., Luhmann, J., & Skoug, R. (2006). Properties of stream interactions at one au during 1995–2004. *Solar Physics*, *239*(1-2), 337–392. doi: https://doi.org/10.1007/s11207-006-0132-3

Joselyn, J., & Tsurutani, B. (1990). Geomagnetic sudden impulses and storm sudden commencements: A note on terminology. *Eos, Transactions American Geophysical Union*, *71*(47), 1808–1809. doi: https://doi.org/10.1029/90EO00350

Juusola, L., Kauristie, K., Amm, O., & Ritter, P. (2009). Statistical dependence of auroral ionospheric currents on solar wind and geomagnetic parameters from 5 years of champ satellite data. In *Annales geophysicae* (Vol. 27, pp. 1005–1017). doi: https://doi.org/10.5194/angeo-27-1005-2009

Kamide, Y., Ahn, B.-H., Akasofu, S.-I., Baumjohann, W., Friis-Christensen, E., Kroehl, H., ... others (1982). Global distribution of ionospheric and field-aligned currents during substorms as determined from six ims meridian chains of magnetometers: Initial results. *Journal of Geophysical Research: Space Physics*, *87*(A10), 8228–8240. doi: https://doi.org/10.1029/JA087iA10p08228

Kamide, Y., Baumjohann, W., Daglis, I., Gonzalez, W., Grande, M., Joselyn, J., ... others (1998b). Current understanding of magnetic storms: Storm-substorm relationships. *Journal of Geophysical Research: Space Physics*, *103*(A8), 17705–17728. doi: https://doi.org/10.1029/98JA01426

Kamide, Y., Baumjohann, W., Daglis, I. A., Gonzalez, W. D., Grande, M., Joselyn, J. A., ... Vasyliunas, V. M. (1998a). Current understanding of magnetic storms: Storm-substorm relationships. *Journal of Geophysical Research: Space Physics*, *103*(A8), 17705-17728. doi: 10.1029/98JA01426

Kamide, Y., Yokoyama, N., Gonzalez, W., Tsurutani, B. T., Daglis, I. A., Brekke, A., & Masuda, S. (1998). Two-step development of geomagnetic storms. *Journal of Geophysical Research: Space Physics*, *103*(A4), 6917-6921. doi: https://doi.org/10.1029/97JA03337

King, J., & Papitashvili, N. (2005). Solar wind spatial scales in and comparisons of hourly wind and ace plasma and magnetic field data. *Journal of Geophysical Research: Space Physics*, *110*(A2). doi: https://doi.org/10.1029/2004JA010649

Korth, H., Anderson, B., & Waters, C. (2010). Statistical analysis of the dependence of large-scale birkeland currents on solar wind parameters. *Annales Geophysicae (09927689)*, *28*(2). doi: https://doi.org/10.5194/angeo-28-515-2010

Krieger, A., Timothy, A., & Roelof, E. (1973). A coronal hole and its identification as the source of a high velocity solar wind stream. *Solar Physics*, *29*(2), 505–525. doi: https://doi.org/10.1007/BF00150828

Laundal, K. M., Reistad, J. P., Finlay, C. C., Østgaard, N., Tenfjord, P., Snekvik, K., & Ohma, A. (2018). Interplanetary magnetic field bx component influence on horizontal and

field-aligned currents in the ionosphere. *Journal of Geophysical Research: Space Physics*, *123*(5), 3360–3379. doi: https://doi.org/10.1002/2017JA024864

Le, G.-M., Liu, G.-A., & Zhao, M.-X. (2020). Dependence of major geomagnetic storm intensity (dst≤ -100 nt) on associated solar wind parameters. *Solar Physics*, *295*(8), 1–9. doi: https://doi.org/10.1007/s11207-020-01675-3

Liu, B.-J., Zhang, X.-X., He, F., & Zong, Q.-G. (2019). The magnetic local time distribution of storm geomagnetic field disturbance under different conditions of solar wind and interplanetary magnetic field. *Journal of Geophysical Research: Space Physics*, *124*(4), 2656–2667. doi: https://doi.org/10.1029/2018JA026287

Loewe, C., & Prölss, G. (1997). Classification and mean behavior of magnetic storms. *Journal of Geophysical Research: Space Physics*, *102*(A7), 14209–14213. doi: https://doi.org/10.1029/96JA04020

McPherron, R., Anderson, B., & Chu, X. (2018). Relation of field-aligned currents measured by the network of iridium® spacecraft to solar wind and substorms. *Geophysical Research Letters*, *45*(5), 2151–2158. doi: https://doi.org/10.1002/2017GL076741

Nakano, S., Ueno, G., Ohtani, S., & Higuchi, T. (2009). Impact of the solar wind dynamic pressure on the region 2 field-aligned currents. *Journal of Geophysical Research: Space Physics*, *114*(A2). doi: https://doi.org/10.1029/2008JA013674

Neupert, W. M., & Pizzo, V. (1974). Solar coronal holes as sources of recurrent geomagnetic disturbances. *Journal of Geophysical Research*, *79*(25), 3701–3709. doi: https://doi.org/10.1029/JA079i025p03701

Newell, P., & Gjerloev, J. (2011a). Evaluation of supermag auroral electrojet indices as indicators of substorms and auroral power. *Journal of Geophysical Research: Space Physics*, *116*(A12). doi: https://doi.org/10.1029/2011JA016779

Newell, P., & Gjerloev, J. (2011b). Substorm and magnetosphere characteristic scales inferred from the supermag auroral electrojet indices. *Journal of Geophysical Research: Space Physics*, *116*(A12). doi: https://doi.org/10.1029/2011JA016936

Newell, P., & Gjerloev, J. W. (2012). Supermag-based partial ring current indices. *Journal of Geophysical Research: Space Physics*, *117*(A5). doi: 10.1029/2012JA017586

Newell, P., Sotirelis, T., Liou, K., & Rich, F. (2008). Pairs of solar wind-magnetosphere coupling functions: Combining a merging term with a viscous term works best. *Journal of Geophysical Research: Space Physics*, *113*(A4). doi: https://doi.org/10.1029/2007JA012825

Palmroth, M., Pulkkinen, T., Janhunen, P., McComas, D., Smith, C., & Koskinen, H. (2004). Role of solar wind dynamic pressure in driving ionospheric joule heating. *Journal of Geophysical Research: Space Physics*, *109*(A11). doi: https://doi.org/10.1029/2004JA010529

Partamies, N., Juusola, L., Tanskanen, E., & Kauristie, K. (2013). Statistical properties of substorms during different storm and solar cycle phases. *Annales Geophysicae (09927689)*, *31*(2). doi: https://doi.org/10.5194/angeo-31-349-2013

Richardson, I. G., & Cane, H. V. (2010). Near-earth interplanetary coronal mass ejections during solar cycle 23 (1996–2009): Catalog and summary of properties. *Solar Physics*, *264*(1), 189–237. doi: https://doi.org/10.1007/s11207-010-9568-6

Richardson, I. G., & Cane, H. V. (2012). Solar wind drivers of geomagnetic storms during more than four solar cycles. *Journal of Space Weather and Space Climate*, *2*, A01. doi: https://doi.org/10.1051/swsc/2012001

Rostoker, G., & Fälthammar, C.-G. (1967). Relationship between changes in the interplanetary magnetic field and variations in the magnetic field at the earth's surface. *Journal of Geophysical Research*, *72*(23), 5853–5863. doi: https://doi.org/10.1029/JZ072i023p05853

Russell, C., & McPherron, R. (1973). Semiannual variation of geomagnetic activity. *Journal of geophysical research*, *78*(1), 92–108. doi: https://doi.org/10.1029/JA078i001p00092

Tanskanen, E., Snekvik, K., Slavin, J., Pérez-Suárez, D., Viljanen, A., Goldstein, M., ... Mursula, K. (2017). Solar cycle occurrence of alfvénic fluctuations and related geo-

efficiency. *Journal of Geophysical Research: Space Physics*, *122*(10), 9848–9857. doi: https://doi.org/10.1002/2017JA024385

Tsurutani, B. T., & Gonzalez, W. D. (1987). The cause of high-intensity long-duration continuous ae activity (hildcaas): Interplanetary alfvén wave trains. *Planetary and Space Science*, *35*(4), 405–412. doi: https://doi.org/10.1016/0032-0633(87)90097-3

Tsurutani, B. T., Gonzalez, W. D., Gonzalez, A. L., Guarnieri, F. L., Gopalswamy, N., Grande, M., ... others (2006). Corotating solar wind streams and recurrent geomagnetic activity: A review. *Journal of Geophysical Research: Space Physics*, *111*(A7). doi: https://doi.org/10.1029/2005JA011273

Tsyganenko, N. A., & Stern, D. P. (1996). Modeling the global magnetic field of the large-scale birkeland current systems. *Journal of Geophysical Research: Space Physics*, *101*(A12), 27187–27198. doi: https://doi.org/10.1029/96JA02735

Turner, N. E., Cramer, W. D., Earles, S. K., & Emery, B. A. (2009). Geoefficiency and energy partitioning in cir-driven and cme-driven storms. *Journal of Atmospheric and Solar-Terrestrial Physics*, *71*(10-11), 1023–1031. doi: https://doi.org/10.1016/j.jastp.2009.02.005

Wang, C., Chao, J., & Lin, C.-H. (2003). Influence of the solar wind dynamic pressure on the decay and injection of the ring current. *Journal of Geophysical Research: Space Physics*, *108*(A9). doi: https://doi.org/10.1029/2003JA009851

Waters, C., Anderson, B., Green, D. L., Korth, H., Barnes, R. J., & Vanhamäki, H. (2020). Science data products for ampere. In M. W. Dunlop & H. Lühr (Eds.), *Ionospheric multi-spacecraft analysis tools: Approaches for deriving ionospheric parameters* (pp. 141–165). Cham: Springer International Publishing. doi: 10.1007/978-3-030-26732-2_7

Waters, C., Anderson, B., & Liou, K. (2001). Estimation of global field aligned currents using the iridium® system magnetometer data. *Geophysical Research Letters*, *28*(11), 2165–2168. doi: https://doi.org/10.1029/2000GL012725

Waters, C., Gjerloev, J., Dupont, M., & Barnes, R. (2015). Global maps of ground magnetometer data. *Journal of Geophysical Research: Space Physics*, *120*(11), 9651–9660. doi: https://doi.org/10.1002/2015JA021596

Webb, D. F., & Howard, R. A. (1994). The solar cycle variation of coronal mass ejections and the solar wind mass flux. *Journal of Geophysical Research: Space Physics*, *99*(A3), 4201–4220. doi: https://doi.org/10.1029/93JA02742

Weigel, R. (2010). Solar wind density influence on geomagnetic storm intensity. *Journal of Geophysical Research: Space Physics*, *115*(A9). doi: https://doi.org/10.1029/2009JA015062

Weimer, D. (2001). Maps of ionospheric field-aligned currents as a function of the interplanetary magnetic field derived from dynamics explorer 2 data. *Journal of Geophysical Research: Space Physics*, *106*(A7), 12889–12902. doi: https://doi.org/10.1029/2000JA000295

Workayehu, A., Vanhamäki, H., & Aikio, A. (2020). Seasonal effect on hemispheric asymmetry in ionospheric horizontal and field-aligned currents. *Journal of Geophysical Research: Space Physics*, *125*(10), e2020JA028051. doi: https://doi.org/10.1029/2020JA028051

Yokoyama, N., & Kamide, Y. (1997). Statistical nature of geomagnetic storms. *Journal of Geophysical Research: Space Physics*, *102*(A7), 14215-14222. doi: https://doi.org/10.1029/97JA00903

Zhang, Y., Sun, W., Feng, X., Deehr, C., Fry, C., & Dryer, M. (2008). Statistical analysis of corotating interaction regions and their geoeffectiveness during solar cycle 23. *Journal of Geophysical Research: Space Physics*, *113*(A8). doi: https://doi.org/10.1029/2008JA013095